Burns & Trauma, 2026, 14, tkag049
https://doi.org/10.1093/burnst/tkag049
Published: 26 July 2026
Research Article

OXFORD

Cryogenic 3D-printed PLGA/nano-selenium scaffold for bone regeneration: a dual-functional strategy synergistically regulating macrophage polarization and osteogenic differentiation

Shengwen Cheng[1,2,3,‡], Yuqiao Wang[1,2,3,‡], Yu Zhai[1,2,3,‡], Mingfei Dong[1,2,3], Xiaole Peng[1,2,3], Xiaohong Luo[4], Jiacheng Liu[1,2,3], Junyan Liu[1,2,3], Yi He[5], Xiaoxiong Li[1,2,3], Ke Huang[1,2,3], Senrui Liu[1,2,3], Fengyuan Liu[6,*], Yuwei Zhang[7], Zhong Alan Li[7,*], Wei Huang[1,2,3,*], Chen Zhao[1,2,3,*], Yiting Lei[1,2,3,7,*]

[1]Department of Orthopedic Surgery, The First Affiliated Hospital of Chongqing Medical University, No. 1 Youyi Road, Yuzhong District, Chongqing, 400016, China
[2]Chongqing Municipal Health Commission Key Laboratory of Musculoskeletal Regeneration and Translational Medicine, No. 1 Youyi Road, Yuzhong District, Chongqing, 400016, China
[3]Orthopedic Research Laboratory of Chongqing Medical University, No. 1 Youyi Road, Yuzhong District, Chongqing, 400016, China
[4]Clinical Medical College and Affiliated Hospital of Chengdu University, No. 82, Section 2, North Second Ring Road, Jinniu District, Chengdu, Sichuan Province, 610081, China
[5]Department of Rehabilitation Medicine, Key Laboratory of Physical Medicine and Precision Rehabilitation of Chongqing Municipal Health Commission, The First Affiliated Hospital of Chongqing Medical University, No. 1 Youyi Road, Yuzhong District, Chongqing, 400016, China
[6]School of Electrical, Electronic and Mechanical Engineering, University of Bristol, Queen's Building, University Walk, Bristol BS8 1TR, United Kingdom
[7]Department of Biomedical Engineering, The Chinese University of Hong Kong, Tai Po Road, Sha Tin District, New Territories, Hong Kong SAR, China

*Corresponding authors. Fengyuan Liu, E-mail: fengyuan.liu@bristol.ac.uk; Zhong Alan Li, E-mail: alanli@cuhk.edu.hk; Wei Huang, E-mail: huangw511@163.com; Chen Zhao, E-mail: lecraz@sina.com; Yiting Lei, E-mail: leiyit614@163.com
‡Shengwen Cheng, Yuqiao Wang, and Yu Zhai contributed equally.

Abstract

Background: **Autologous and allogeneic bone grafts are primarily used for bone tissue defects; however, they have limitations such as limited supply, donor site morbidity, and immune rejection risks. Therefore, substitute synthetic bone grafts are required. This study aims to develop a cryogenic 3D-printed PLGA/HA@SeNPs scaffold that synergistically regulates macrophage polarization and osteogenic differentiation for bone regeneration.**

Methods: **Using low-temperature 3D printing combined with freeze-drying technology, a hierarchically porous PLGA/HA@SeNPs composite scaffold was fabricated by compositing poly(lactic-co-glycolic acid) (PLGA) with hyaluronic acid-modified selenium (Se) nanoparticles (HA@SeNPs), enabling sustained immunomodulation and osteogenic activity through its engineered microtopography and bioactive components.**

Results: In vitro **evaluations confirmed that the unique microstructure and sustained Se release from HA@SeNPs synergistically promoted macrophage polarization toward the M2 phenotype, accompanied by enhanced osteogenic differentiation as shown by upregulation of Runx2 and osteocalcin and accelerated matrix mineralization. Implantation into a rat femoral critical-sized defect model resulted in substantially improved bone repair and architectural restoration.**

Conclusions: **These findings indicate that the intrinsic physicochemical properties of the PLGA/HA@SeNPs scaffold orchestrate a favorable osteo-immune environment, positioning it as a promising platform for bone regeneration.**

Keywords Cryogenic 3D printing, Nano-selenium, Immunomodulation, Bone regeneration; Macrophage polarization; Osteogenesis

Received: 13 January 2026. **Revised:** 2 July 2026. **Accepted:** 24 July 2026
© The Author(s) 2026. Published by Oxford University Press.
This is an Open Access article distributed under the terms of the Creative Commons Attribution-NonCommercial License (https://creativecommons.org/licenses/by-nc/4.0/), which permits non-commercial re-use, distribution, and reproduction in any medium, provided the original work is properly cited. For commercial re-use, please contact reprints@oup.com for reprints and translation rights for reprints. All other permissions can be obtained through our RightsLink service via the Permissions link on the article page on our site—for further information please contact journals.permissions@oup.com.

Downloaded from academic.oup.com/burnstrauma/article/doi/10.1093/burnst/tkag049/8742059 by guest on 12 October 2026

Highlights

- Cryogenic 3D-printed poly(lactic-co-glycolic acid)/hyaluronic acid-modified selenium nanoparticles scaffold with hierarchical microporous topography.
- Synergistic immunomodulation *via* microstructural cues and sustained selenium release driving M2 macrophage polarization.
- Enhanced osteogenic differentiation of bone marrow mesenchymal stem cells through mitogen-activated protein kinase signaling pathway activation.
- Significant bone regeneration in rat critical-sized femoral defects *via* drug-free osteo-immunomodulation.
- A promising immunomodulatory biomaterial platform for bone tissue engineering.

Background

Bone tissue defects affect millions of patients worldwide each year and present a substantial challenge in orthopedic surgery [1–3]. In particular, traumatic bone defects caused by open fractures, polytrauma, or blast injuries are associated with exacerbated and prolonged inflammatory responses, which further compromise bone healing. Although autologous and allogeneic bone grafts remain the clinical standard, their utility is constrained by inherent limitations, including limited availability, donor-site morbidity, and the risk of immune rejection [4–6]. Recent advances in biomaterials and nanomedicine have provided a wide array of synthetic strategies for bone regeneration, including nanoparticle-based delivery systems, engineered scaffolds, and molecular/cellular approaches [7–12]. Thus, the development of synthetic bone graft substitutes has become a central focus in regenerative medicine [13–15]. In addition to providing osteoconductive scaffolds, successful bone regeneration is now recognized as a process requiring intricate cooperation between the skeletal and immune systems [16, 17]. This cooperation is especially critical in trauma- or burn-related bone defects, where the local immune environment is often dominated by persistent inflammation [18]. In this complex microenvironment, macrophages are pivotal orchestrators during the early healing phase [19, 20]. However, their functional plasticity dictates the repair outcome: the pro-inflammatory M1 phenotype can perpetuate inflammation and impede healing through the secretion of cytokines, such as tumor necrosis factor-alpha (TNF-α) and interleukin (IL)-6 [21], whereas the anti-inflammatory M2 phenotype promotes tissue remodeling and immune homeostasis *via* factors, such as IL-10 [22]. Consequently, the strategic reprogramming of macrophage polarization from a pro-inflammatory M1 to pro-regenerative M2 state has emerged as a promising therapeutic paradigm to ameliorate inflammation and actively foster osteogenesis, marking a decisive shift from an “immune-evasive” to “immune-reprogramming” biomaterial design [23].

Within this immunomodulatory paradigm, poly(lactic-co-glycolic acid) (PLGA) has been extensively investigated as a foundational biomaterial for bone repair owing to its well-documented biocompatibility, tunable degradation kinetics, and Food and Drug Administration approval for clinical use [24]. However, pristine PLGA scaffolds are largely bioinert and lack the inherent capacity to direct macrophage polarization or actively stimulate osteogenic differentiation, often resulting in a suboptimal immune response and limited regenerative outcomes [25]. While selenium (Se) is an essential trace element that plays a vital role in cellular redox regulation and antioxidant defense, its conventional forms face significant clinical limitations, such as a narrow therapeutic window and potential toxicity [26–29]. In our previous study, selenium nanoparticles (SeNPs) were shown to overcome these drawbacks and exert multifaceted antioxidant effects by directly scavenging reactive oxygen species (ROS), promoting endogenous selenoprotein synthesis, and improving mitochondrial function, offering a novel therapeutic strategy for oxidative stress-related diseases such as osteoarthritis [30]. However, the therapeutic application of bare SeNPs is frequently hampered by their colloidal instability and potential toxicity. To overcome these challenges, the surfaces of SeNPs have been modified with biopolymers such as hyaluronic acid (HA). The formation of a protective HA corona not only significantly enhances the colloidal and physiological stability of SeNPs, preventing their aggregation and ensuring a more predictable pharmacokinetic profile, but also confers additional bioactive functions, such as enhancing targeted delivery to immune cells through CD44 receptor interactions [31–33]. Furthermore, studies investigating the role of Se in bone metabolism have suggested that it regulates osteogenic differentiation through antioxidant defense-related pathways [34, 35]. The strategic incorporation of SeNPs into a PLGA matrix creates a synergistic system in which the polymer provides structural support and enables the controlled release of Se species, thereby effectively overcoming the limitations of rapid clearance and potential toxicity associated with free Se compounds [36].

To overcome the limitations of conventional 3D printing for fabricating bioactive nanocomposite scaffolds, cryogenic 3D printing technology has been introduced [37, 38]. Traditional methods often involve high temperatures or organic solvents, which can degrade or compromise the functionality of thermosensitive bioactive components such as SeNPs. In contrast, cryogenic 3D printing, performed at low temperatures, preserves the stability and bioactivity of the incorporated SeNPs while enabling precise architectural control of the scaffold [39, 40]. This advanced manufacturing approach facilitates the fabrication of patient-specific constructs with predetermined geometries that closely match bone defect contours. More importantly, it enables precise regulation of critical parameters, including pore size, interconnectivity, and surface topography, all of which are essential for bone regeneration. These physical cues are not merely passive; they actively participate in immune regulation. The specific microtopography generated by the cryogenic process directly influences macrophage adhesion and morphology, predisposing macrophages toward the pro-healing M2 phenotype [41, 42]. This engineered microenvironment creates a powerful

Downloaded from academic.oup.com/burnstrauma/article/doi/10.1093/burnst/tkag049/8742059 by guest on 12 October 2026

synergistic effect when combined with the sustained release of Se from the nanoparticles. Notably, this system promotes bone regeneration through the intrinsic properties of the material itself, without relying on exogenous drugs. The topography of the scaffold provides the initial "physical instruction" to immune cells, while the bioactive SeNPs provide sustained "biochemical reinforcement" *via* immunomodulatory and redox-mediated pathways. Together, they directly orchestrate a robust and durable M2-polarized milieu. This favorable immune landscape secretes osteo-inductive cytokines (e.g., BMP-2) that directly enhance the osteogenic differentiation of mesenchymal stem cells, thereby bridging early-stage immunomodulation with subsequent bone formation through a direct, drug-free material-based strategy [43, 44].

This integrated approach combines cryogenic 3D printing with the incorporation of SeNPs into a hierarchically porous PLGA/HA composite, enabling precise control of scaffold architecture and sustained immunomodulatory release. Figure 1 illustrates that the PLGA/HA@SeNPs scaffold leverages engineered microtopography and controlled Se release to direct macrophage polarization toward the M2 phenotype and enhance osteogenic differentiation. This strategy creates a unified platform that synchronizes immune microenvironment remodeling with bone formation while mimicking the native bone structure and providing osteoimmunomodulatory signals. This approach directly addresses the unmet need for biomaterials that can simultaneously regulate trauma-induced immune dysregulation and promote bone healing, offering a promising osteoimmunomodulatory strategy for burn- and trauma-related bone defects.

Methods

Materials

The materials for fabricating the composite scaffolds included PLGA (lactide:glycolide = 75:25, Mw ≈ 200 000 Da; Jinan Daigang Biomaterial Co., Ltd.), hydroxyapatite nanoparticles (~50 nm; Macklin Biochemical Co., Ltd.), and the solvent dichloromethane (Chron Chemicals Co., Ltd.). Sodium selenite (Na_2SeO_3) was supplied by Macklin Biochemical Co., Ltd. (Shanghai, China); ascorbic acid and L-glutathione (reduced) were obtained from Sigma-Aldrich (St. Louis, MO, USA). For the *in vitro* biological evaluations, the THP-1 murine macrophage cell line and bone marrow mesenchymal stem cells (BMSCs) were procured from the Chinese Academy of Sciences Cell Bank (Shanghai, China). Roswell Park Memorial Institute medium (RPMI), Alpha Minimum Essential Medium (α-MEM), fetal bovine serum (FBS), and penicillin–streptomycin were purchased from Gibco (Grand Island, NY, USA). Cell Counting Kit-8 (CCK-8), calcein-AM/propidium iodide (PI) dual fluorescence kit, alkaline phosphatase (ALP) Staining Kit, Alizarin red Staining (ARS), Antifade Mounting Medium with 4′,6-diamidino-2-phenylindole (DAPI), radioimmunoprecipitation assay (RIPA) lysis buffer, and Radioimmunoprecipitation assay (PMSF) solution were all obtained from Beyotime Biotechnology Co., Ltd. (Shanghai, China). Additionally, enzyme-linked immunosorbent assay (ELISA) kits were supplied by Jiangsu Aidisheng Biological Technology Co., Ltd. (Nanjing, China). For protein analysis, Western blotting reagents were sourced as follows: NcmBlot Rapid Transfer Buffer (20×) and Universal Antibody Diluent were provided by NCM Biotech (Suzhou, China); UniTM SDS PAGE Running Buffer (50×) was acquired from affinibody (Wuhan, China); 5× sodium dodecyl sulfate–polyacrylamide gel electrophoresis (SDS-PAGE) sample loading buffer and other Western blot reagents were purchased from Biyuntian Biotechnology Co., Ltd. (Shanghai, China). All specific antibodies and primer sequences for reverse transcription-quantitative polymerase chain reaction (RT-qPCR) used in this study are detailed in Tables S1 and S2, respectively.

Preparation of HA@NeNPs

Based on our previously established protocol, hyaluronic acid-modified selenium nanoparticles (HA@SeNPs) were synthesized using an in situ reduction method. Briefly, 500 mg of HA was uniformly dispersed in 100 mL of deionized water by ultrasonication for 30 min. Next, 100 mL of an aqueous solution containing 10 mM sodium selenite (Na_2SeO_3) was added dropwise to the HA suspension under continuous stirring. After stirring for 1 h, 20 mL of a 50 mM ascorbic acid solution was added to reduce selenite ions to elemental Se, thereby inducing the nucleation and growth of SeNPs on the HA surface. The reaction was allowed to proceed for 6 h at room temperature under constant stirring. The resulting HA@SeNP composite was collected by centrifugation at 10,000 rpm for 10 min, washed three times with deionized water and absolute ethanol to remove unreacted precursors, and finally lyophilized for 48 h. The successful synthesis of the HA@SeNPs was confirmed by transmission electron microscopy (TEM), X-ray diffraction (XRD), and X-ray photoelectron spectroscopy (XPS).

3D printing of PLGA/HA@SeNPs scaffolds

A homogeneous bioink was formulated by dissolving PLGA in dioxane at a concentration of 20% (w/v). HA@SeNPs powder was then incorporated into the PLGA solution at concentrations of 5%, 10%, and 15% (w/w, relative to PLGA) to investigate the effect of Se content. The mixture was magnetically stirred for 6 h, followed by ultrasonication in an ice bath for 30 min to achieve a uniform dispersion. Scaffold fabrication was performed using a low-temperature deposition manufacturing 3D printing system (BioScaffolder 3.0, GeSiM, Germany) with the following optimized parameters: a nozzle diameter of 0.35 mm (23G), a printing pressure of 100 kPa, a printing speed of 5 mm/s, a layer height of 0.35 mm, and a printing temperature maintained at 10 °C. The printed scaffolds were subsequently freeze-dried for 48 h to remove residual solvent and stored in a desiccator until further use.

Characterization of the PLGA/HA@SeNPs scaffolds

The morphology and internal microstructure of the scaffolds were observed using scanning electron microscopy (SEM, ZEISS Sigma360, Germany) and High-Resolution Transmission Electron Microscopy (HRTEM, FEI Tecnai G2 F30, USA). The morphology of cells on the scaffolds was examined using scanning electron microscopy (SEM, Hitachi SU8100, Japan).Elemental distribution was observed through energy-dispersive X-ray spectroscopy scanning (EDS, Oxford Xplore30, UK). The chemical structure and

Downloaded from academic.oup.com/burnstrauma/article/doi/10.1093/burnst/tkag049/8742059 by guest on 12 October 2026

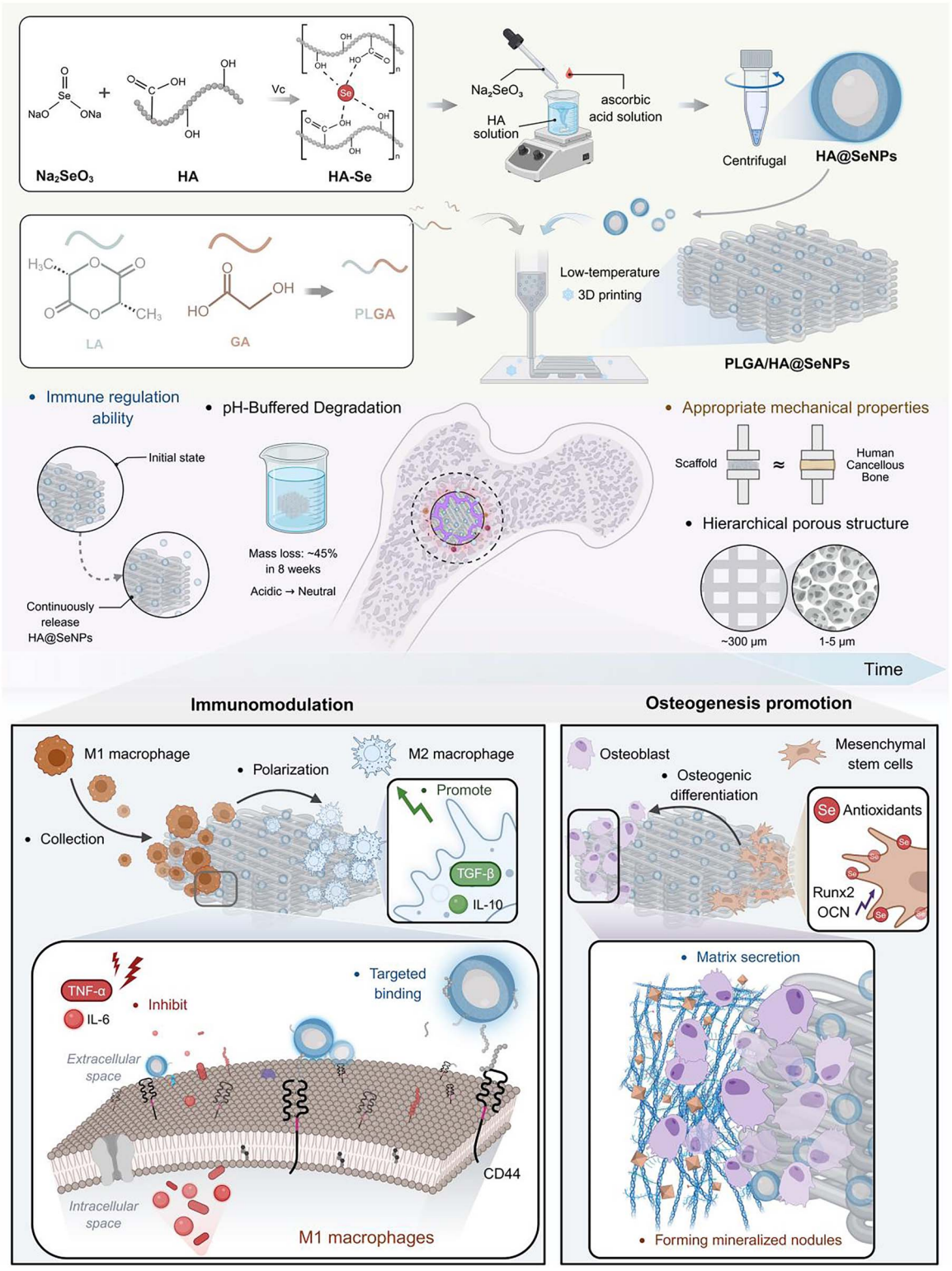


Figure 1 Schematic representation of the fabrication process and osteogenic-immunomodulatory mechanism of the PLGA/HA@SeNPs composite scaffold. *PLGA/HA@SeNPs* poly(lactic-co-glycolic acid)/hyaluronic acid-modified selenium nanoparticles

phase composition were analyzed by Fourier transform infrared spectroscopy (FTIR, Nicolet iS50, Thermo Scientific, USA), XRD (Rigaku Ultima IV, Japan) and differential scanning calorimetry (DSC, NETZSCH STA 449 F3, Germany). The water contact angle was measured using a contact angle goniometer (Dataphysics OCA50, Germany) to assess surface wettability. The elemental content in liquids was detected using inductively coupled plasma (ICP, Thermo ICP-MS, USA).

Downloaded from academic.oup.com/burnstrauma/article/doi/10.1093/burnst/tkag049/8742059 by guest on 12 October 2026

In vitro degradation and selenium release profile

Scaffold degradation and Se release were evaluated by immersing the scaffold samples in 10 mL of phosphate-buffered saline (PBS, pH 7.4) at 37 °C under gentle shaking (60 rpm). At predetermined time points (1, 3, 7, 14, 21, and 28 days), the supernatant was collected and replaced with fresh PBS. The concentration of released Se was quantified by ICP-MS (Agilent 7800, USA), whereas scaffold mass loss was determined by weighing the samples before and after degradation. In addition, the pH of the degradation medium was monitored throughout the experiment.

To evaluate the long-term Se release profile and biosafety, the release study was extended to 56 days. At the end of the 56-day period, the supernatant was collected, and the Se concentration was determined by ICP-MS (PerkinElmer NexION 300D, USA). For sample preparation, 1 mL of the collected supernatant was mixed with 1 mL of nitric acid and heated at 120 °C for approximately 30 min to digest the sample. After cooling, the mixture was diluted to a fixed volume, and the Se concentration was measured.

Cytocompatibility and macrophage response assessment

The cytocompatibility of the scaffolds was evaluated using the CCK-8 assay and live/dead staining according to ISO 10993-5. To determine the optimal HA@SeNPs concentration for subsequent experiments, PLGA/HA@SeNPs scaffolds containing different HA@SeNPs contents (1%, 2%, 5%, 8%, and 10% w/w relative to PLGA) were fabricated. Their cytocompatibility was assessed by culturing BMSCs with scaffold extracts for 1, 3, and 5 days. Human THP-1 cells were first differentiated into M0 macrophages by treatment with 100 ng/ml phorbol 12-myristate 13-acetate (PMA) for 24 h. The resulting adherent macrophages were cultured in RPMI supplemented with 10% FBS. Scaffold extracts were prepared by incubating samples in a complete medium at 37°C for 24 h at a ratio of 1 cm^2/ml. Cells were exposed to the extracts for 1, 3, and 5 days, and cell viability was measured using the CCK-8 kit. For macrophage polarization studies, the differentiated THP-1 macrophages were cultured with scaffold extracts and then stimulated with LPS (100 ng/mL) for an additional 24 h. Total RNA was subsequently extracted from the cells for RT-PCR analysis. The expression of M1 (CD86, iNOS) and M2 (CD206, Arg-1) markers was analyzed using RT-PCR along with immunofluorescence, with transcript levels of Arg1, iNOS, Cd86, and Cd206 quantified, normalized to Gapdh, and calculated *via* the $2^{\wedge}(-\Delta\Delta Ct)$ method using GraphPad Prism (v9.0). Data are derived from triplicate biological replicates, and statistical significance was defined as $P < .05$. Total protein was extracted from the cells using RIPA lysis buffer containing PMSF (Biostar Biotechnology Co., Ltd., Shanghai, China) under ice conditions. Protein concentration was determined using the bicinchoninic acid protein concentration assay kit (Biostar Biotechnology Co., Ltd., Shanghai, China). Equal amounts of protein were then loaded and separated on 10% SDS-PAGE gel, followed by transfer to polyvinylidene fluoride (PVDF) membrane. The membrane was then blocked with 5% defatted milk in Tris-buffered saline (TBST) containing Tween-20 for 1 h and then washed with TBST three times. The membrane was then incubated with the primary antibody targeting the protein of interest at 4°C overnight. After washing with TBST three times, incubate the membrane with the secondary antibody (Abcam Inc., Cambridge, MA, USA) at room temperature for 1 h. Finally, detect the protein bands using the enhanced chemiluminescence (ECL) detection system (Mishu Biotechnology Co., Ltd., Xi'an, China) and analyze them with Image J software (National Institutes of Health, Bethesda, MD, USA). For immunofluorescence staining, the cells were fixed with 4% paraformaldehyde. Subsequently, the samples were permeabilized with a 0.1% Triton X-100 solution for 15 min and blocked with 5% goat serum for 30 min. Thereafter, the cells were incubated with primary antibodies overnight at 4°C. Following incubation with fluorescently-conjugated secondary antibodies, the actin cytoskeleton was stained with TRITC Phalloidin, and the cell nuclei were counterstained with DAPI. Images were captured using a fluorescence microscope (Olympus DP74, Olympus Corporation, Tokyo, Japan), and fluorescence intensity was quantified with ImageJ software (National Institutes of Health, Bethesda, MD, USA). To evaluate the macrophage cytokine secretion profile, the secreted levels of TNF-α and IL-6 were measured, as well as the IL-10/TNF-α ratio, using commercial ELISA kits (Jiangsu Aidisheng Biological Technology Co., Ltd., Nanjing, China) according to the manufacturer's instructions.

Osteoimmunomodulatory activity and osteogenic differentiation evaluation

To investigate the osteoimmunomodulatory effects of the scaffolds, conditioned medium (CM) was collected from THP-1 macrophages cultured on the scaffolds for 3 days. BMSCs were then cultured in the CM for 7 and 14 days. ALP activity was assessed on day 7 using an ALP staining kit. Matrix mineralization was evaluated on day 14 by ARS staining. The expression of osteogenic genes (Runx2, Opn, Ocn, and Col1a1) was analyzed by RT-qPCR. To further evaluate the osteogenic differentiation potential of the scaffolds, BMSCs were also analyzed by RT-qPCR and immunofluorescence staining following the protocol described above.

Transcriptomic analysis and validation

To elucidate the molecular mechanisms underlying the enhanced osteogenic differentiation induced by the PLGA/HA@SeNPs scaffold, transcriptomic profiling was performed. BMSCs were cultured in control medium or medium containing PLGA/HA@SeNPs scaffold extracts for 7 days. Total RNA was extracted using TRIzol reagent, and RNA sequencing was performed using the Illumina NovaSeq 6000 platform. Differentially expressed genes were identified, followed by Kyoto Encyclopedia of Genes and Genomes (KEGG) pathway enrichment analysis and Gene Set Enrichment Analysis (GSEA) to identify significantly enriched signaling pathways. Based on the enriched pathways, the expression of key proteins involved in the relevant signaling pathways was further validated by Western blotting and immunofluorescence staining.

In vivo experiment

All animal procedures were approved by the Institutional Animal Care and Use Committee of Chongqing Medical University (Approval No.IACUC-CQMU-2024-0382). A rat femoral condyle

Downloaded from academic.oup.com/burnstrauma/article/doi/10.1093/burnst/tkag049/8742059 by guest on 12 October 2026

defect model was established using Sprague–Dawley rats (12 weeks old, male). The sample size of five animals per group ($n = 5$) was determined based on well-established rodent femoral condyle defect models, which have been shown to provide adequate statistical power for detecting significant differences in bone regeneration outcomes. In accordance with the ARRIVE guidelines, 20 animals were randomly assigned to four experimental groups ($n = 5$ per group) using a computer-based online random number generator (GraphPad QuickCalcs; https://www.graphpad.com/quickcalcs/randomize1/) to ensure unbiased allocation. Critical-sized defects (5 mm in diameter, 5 mm in depth) were created and implanted with the following groups: (i) blank control, (ii) PLGA scaffold, (iii) PLGA/HA scaffold, and (iv) PLGA/HA@SeNPs scaffold ($n = 5$ per group). After 6 and 12 weeks, the rats were euthanized, and femurs were harvested for micro-computed tomography (micro-CT) scanning (Scanco μCT 100, Switzerland) to evaluate bone regeneration parameters, including bone volume/total volume (BV/TV), trabecular number (Tb.N), and trabecular separation (Tb.Sp). Histological analysis was performed using hematoxylin and eosin (H&E) staining and Masson's trichrome staining. For immunofluorescence staining, the sections were treated with 0.3% Triton X-100 and blocked with 5% goat serum. The sections were then incubated overnight with primary antibodies against collagen type I alpha 1 (Col1α1), TNF-α, Osterix (OSX), and CD206. After primary antibody incubation, the slides were washed and incubated with secondary antibodies at room temperature for 1 h. The nuclei were stained with DAPI, and images were captured using a fluorescence microscope (Olympus DP74, Olympus Corporation, Tokyo, Japan). All immunohistochemical and immunofluorescence images were quantitatively analyzed and statistically evaluated using Image J software (National Institutes of Health, Bethesda, MD, USA). In addition, to assess systemic biocompatibility, major organs (heart, liver, spleen, lungs, and kidneys) were collected at the endpoint and stained with H&E.

Statistical analysis

All data are presented as the mean $\pm$ standard deviation. Statistical analyses were performed using GraphPad Prism (version 9.0). One-way analysis of variance followed by Tukey's post hoc test was used for multiple-group comparisons. A p value < 0.05 was considered statistically significant.

Results

Fabrication and physicochemical evaluation of PLGA/HA@SeNPs composite scaffolds

Synthesis and characterization of HA@SeNPs hybrids

HA@SeNPs were synthesized using a redox-precipitation method under controlled conditions to ensure uniform nanoparticle formation and effective HA functionalization. This key bioactive component was then integrated into the structural polymer PLGA and fabricated into a porous scaffold by cryogenic 3D printing, as illustrated in the overall fabrication process (Figure 2a). This process resulted in the progressive development of a homogeneous orange-red colloidal dispersion, confirming the formation of SeNPs stabilized within the HA matrix (Figure 2b).

Morphological assessment by TEM confirmed the formation of spherical nanoparticles within the nanometer size range (Figure 2c). Dynamic light scattering analysis indicated a narrow particle size distribution with a mean hydrodynamic diameter of 406 $\pm$ 27 nm, whereas zeta potential analysis showed a surface charge of -30.5 ± 0.2 mV, reflecting the colloidal stabilization imparted by the anionic HA chains (Figure 2d and e). To verify the successful surface modification of SeNPs with HA and evaluate its potential influence on the oxidation state of Se, XPS was performed on both unmodified SeNPs and HA@SeNPs. The survey XPS spectra exhibited a distinct nitrogen (N) signal only in the HA@SeNPs sample (Figure 2f), attributable to the nitrogen-containing amide groups of HA. High-resolution N 1s spectra further revealed characteristic peaks at binding energies of approximately 399.8 eV and 401.2 eV, corresponding to –NH–C=O and –N–C=O moieties, respectively, confirming the successful conjugation of HA to the SeNP surface through amide linkages (Figure 2g and h). In parallel, the high-resolution Se 3D spectra displayed nearly identical profiles for both SeNPs and HA@SeNPs, demonstrating that HA modification did not alter the oxidation state of Se, which remained in the zero-valent (Se^0) form (Figure 2i and j). These results indicate that HA functionalization was confined to the nanoparticle surface without affecting the intrinsic chemical properties of the SeNPs.

Cryogenic 3D printing process optimization and scaffold manufacturing

The PLGA copolymer used in this study was first characterized by gel permeation chromatography. The chromatogram revealed a major peak accounting for 81.04% of the total peak area, with a number-average molecular weight of 190,872 g/mol and a Mw of 250,399 g/mol, yielding a polydispersity index of 1.31. These molecular parameters indicate a relatively narrow and homogeneous molecular weight distribution, which is characteristic of PLGA synthesized by ring-opening polymerization and contributes to its suitable melt viscosity and processability for cryogenic 3D printing (Table S3). PLGA/HA@SeNPs composite scaffolds were fabricated *via* cryogenic 3D printing, a process schematically (Figure 3a), following systematic optimization of both the material composition and the processing parameters. To preserve the bioactivity of the incorporated HA@SeNPs while achieving precise extrusion, the printability of the composite inks was first evaluated under a controlled temperature gradient. A printing temperature of 37 °C was identified as optimal, providing sufficient ink fluidity without compromising the stability or bioactivity of the thermosensitive SeNPs. Bioinks containing varying concentrations of HA@SeNPs (2%, 5%, 8%, and 10% w/w, relative to PLGA) were prepared to evaluate their printability (Figure 3b). When the HA@SeNPs concentration exceeded 10%, the substantially increased viscosity of the composite ink compromised extrusion continuity and structural fidelity, resulting in inconsistent filament deposition and occasional nozzle clogging. The printing process was performed under precisely controlled thermal conditions: the printing cartridge temperature was maintained between 25 and 37 °C to ensure optimal ink fluidity, whereas the receiving platform was maintained at −5 °C to enable the immediate freezing of the deposited filaments.

Downloaded from academic.oup.com/burnstrauma/article/doi/10.1093/burnst/tkag049/8742059 by guest on 12 October 2026

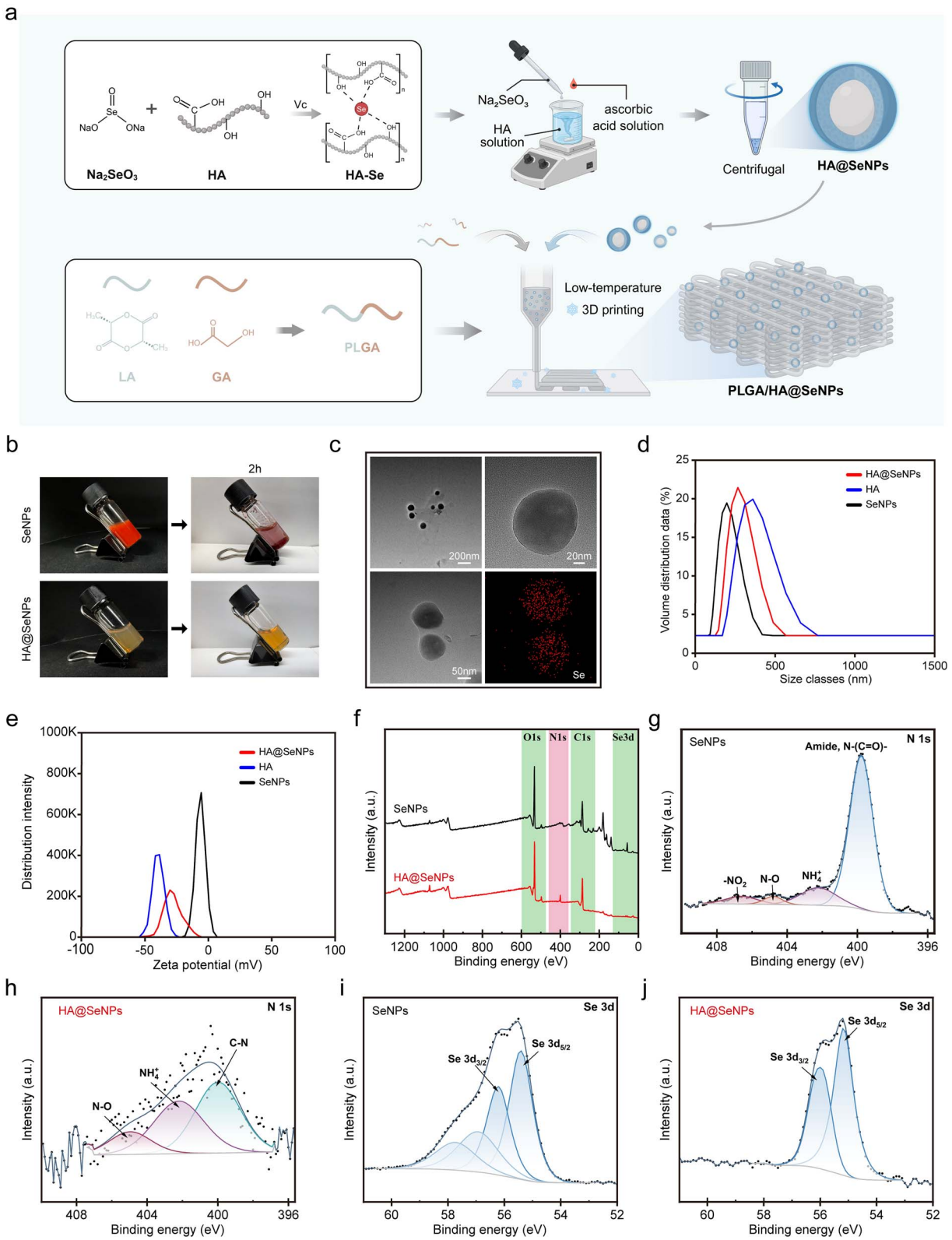


Figure 2 Synthesis and structural characterization of HA@SeNPs. (**a**) Schematic of the fabrication process for the PLGA/HA@SeNPs scaffold. (**b**) Photograph of the homogeneous orange-red colloidal dispersion of HA@SeNPs. (**c**) TEM image showing spherical HA@SeNPs. Scale bar: 20 nm, 50 nm and 200 nm. (**d**) Hydrodynamic size distribution of SeNPs and HA@SeNPs measured by DLS. (**e**) Zeta potential of SeNPs and HA@SeNPs. (**f**) XPS survey spectra of SeNPs and HA@SeNPs. (**g**) High-resolution N 1 s XPS spectrum of SeNPs. (**h**) High-resolution N 1 s XPS spectrum of HA@SeNPs. (**i**) High-resolution Se 3D XPS spectrum of SeNPs. (**j**) High-resolution Se 3D XPS spectrum of HA@SeNPs. Data are expressed as mean ± SD. *HA* hyaluronic acid, *SeNPs* selenium nanoparticles, *PLGA* poly(lactic-co-glycolic acid), *TEM* transmission electron microscopy, *DLS* dynamic light scattering, *XPS* X-ray photoelectron spectroscopy, *SD* standard deviation

Downloaded from academic.oup.com/burnstrauma/article/doi/10.1093/burnst/tkag049/8742059 by guest on 12 October 2026

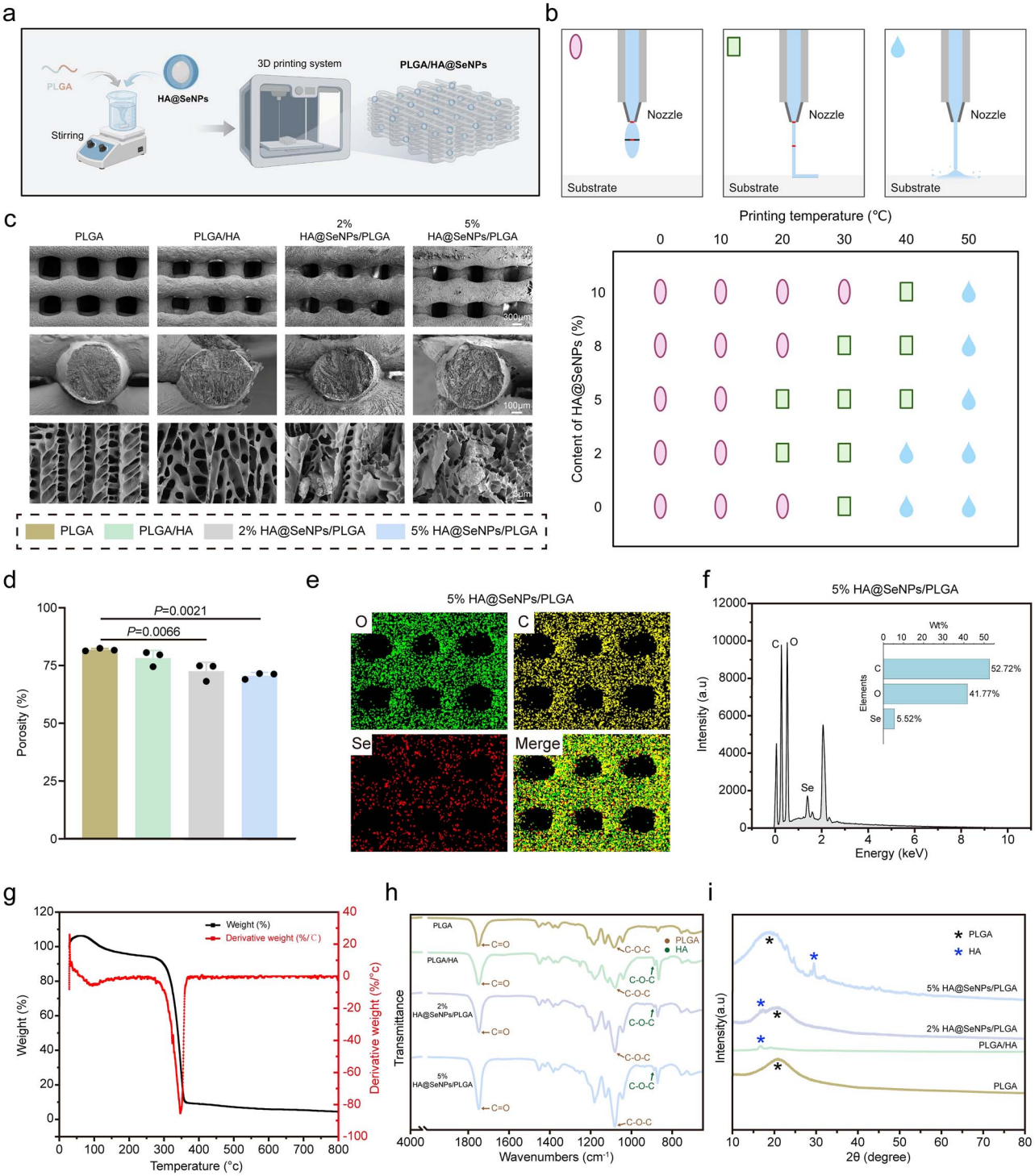


Figure 3 Cryogenic 3D printing process and structural characterization of the PLGA/HA@SeNPs scaffolds. (**a**) Schematic of the cryogenic 3D printing setup. (**b**) Evaluation of the printability of bioinks with varying HA@SeNPs concentrations (2%, 5%, 8%, and 10% w/w relative to PLGA). (**c**) SEM images at different magnifications showing the hierarchical porous architecture and surface microtopography of the scaffold. Scale bar: 3 μm, 100 μm and 300 μm. (**d**) Measured porosity of scaffolds with different HA@SeNPs contents (0–10 wt%). (**e**) EDS elemental mapping of the scaffold. (**f**) EDS point analysis of the 5% HA@SeNPs/PLGA composite scaffold. (**g**) TGA curves of the composite scaffolds. (**h**) FTIR spectra of PLGA,PLGA/HA, the 2% and 5% HA@SeNPs/PLGA composite scaffolds. Characteristic peaks of PLGA and HA are highlighted in yellow and green, respectively. (**i**) XRD patterns of PLGA, and the 2% and 5% HA@SeNPs/PLGA composite scaffolds. Characteristic signals of PLGA and HA@SeNPs are indicated by black symbols and blue symbols, respectively. Data are expressed as mean ± SD. *PLGA* poly(lactic-co-glycolic acid), *HA* hyaluronic acid, *SeNPs* selenium nanoparticles, *SEM* scanning electron microscopy, *EDS* energy-dispersive spectroscopy, *TGA* thermogravimetric analysis, *FTIR* fourier transform infrared spectroscopy, *XRD* X-ray diffraction, *SD* standard deviation

Downloaded from academic.oup.com/burnstrauma/article/doi/10.1093/burnst/tkag049/8742059 by guest on 12 October 2026

Multi-scale architectural and compositional characterization

SEM revealed that the cryogenically printed scaffolds possessed a hierarchically porous architecture with a microscale surface topography. At lower magnification, the scaffolds displayed regular grid patterns with interconnected macropores averaging at 661 ± 12 μm in diameter. Higher magnification images showed micro-scale roughness on the filament surfaces, which was attributed to the incorporated HA@SeNPs and unique solidification behavior under cryogenic conditions. The microporous surface structure, characterized by 1–5-μm pores, provided increased surface area for cell attachment and interaction (Figure 3c). This sophisticated architectural design creates distinct but interconnected biological compartments; the macroporous network supports rapid vascularization and spatial organization of new tissue formation, whereas the micro-textured surfaces significantly increase the available area for cell adhesion and paracrine signaling [45]. More importantly, this multi-scale topological strategy establishes specialized microenvironments that can simultaneously accommodate different cellular processes. Macrophages can interact with the micro-scale features to initiate favorable immunomodulatory responses, whereas mesenchymal stem cells can use macroporous spaces for osteogenic differentiation [46, 47].

Porosity measurements revealed that the scaffolds exhibited a highly porous structure, with total porosity values ranging from 69% to 82%, which were inversely correlated with the HA@SeNPs content (0–5 wt%). The optimal composition containing 5% HA@SeNPs exhibited a porosity of 71 ± 2%, which falls within the ideal range for cancellous bone regeneration and facilitates efficient nutrient diffusion and metabolic waste removal (Figure 3d). This porous architecture (50–90% porosity) satisfies the requirements for cancellous bone by balancing nutrient transport and structural stability [48]. Elemental mapping by EDS confirmed the homogeneous distribution of Se throughout the scaffold architecture, indicating the successful integration and uniform dispersion of HA@SeNPs within the PLGA matrix. The Se signal exhibited a consistent spatial correlation with carbon and oxygen, confirming the stable incorporation of the nanoparticles without aggregation or phase separation (Figure 3e). Furthermore, EDS point analysis of the 5% HA@SeNPs/PLGA composite also confirmed the homogeneous distribution of Se (Figure 3f). Thermogravimetric analysis (TGA) was performed to evaluate the thermal stability and composition of the composite scaffolds. The TGA curves exhibited a characteristic two-stage degradation profile: an initial minor mass loss (∼5%) below 200 °C, attributed to moisture evaporation, followed by a major decomposition event between 250 and 400 °C, corresponding to PLGA polymer chain degradation. The residual mass at 600 °C progressively increased with increasing HA@SeNPs content, reaching 4.4 ± 0.04% for the 5% composite, confirming the successful incorporation and thermal stability of the inorganic components within the PLGA matrix (Figure 3g).

FTIR analysis provided direct evidence for the successful fabrication of the PLGA/HA@SeNPs composite scaffolds. The spectra exhibited characteristic absorption bands corresponding to each component, confirming their successful integration. The characteristic absorption bands of PLGA, including the strong C=O stretching vibration at ∼1750 cm-1 and the C–O–C stretching vibration (primarily arising from ester linkages) at ∼1080 cm-1, were consistently observed in all composite spectra. Importantly, a new characteristic band emerged at ∼890 cm-1 in the composite scaffolds, which was absent in pure PLGA. This band is a well-established spectral fingerprint of the C–O–C linkage within the β-glycosidic bonds of the HA backbone (Figure 3h). The appearance of this HA-specific fingerprint band, together with its increasing intensity as the HA@SeNPs loading increased, confirms the successful incorporation of HA@SeNPs into the PLGA matrix. To further elucidate the structural characteristics of the composite scaffolds, XRD analysis was performed. The diffraction pattern of pure PLGA exhibited a broad amorphous halo centered at 2θ = ∼20.9°, characteristic of its amorphous structure. Following the incorporation of HA@SeNPs, the composite scaffolds retained the dominant amorphous characteristics of PLGA, confirming that HA@SeNPs were successfully incorporated without disrupting the overall amorphous matrix. Notably, in the scaffold containing 5% HA@SeNPs, an additional diffraction peak emerged at 2θ = ∼29.5°, which was attributed to the characteristic diffraction signal of HA@SeNPs within the composite. The absence of this peak in the 2% HA@SeNPs group was attributed to the effective encapsulation of the lower HA@SeNPs content within the PLGA matrix. Collectively, these structural features verify the successful fabrication of the PLGA/HA@SeNPs composite scaffold, whose tunable composition may influence its degradation behavior and Se release profile for tissue engineering applications (Figure 3i).

Mechanical properties, degradation, and biomimernalization behaviors

A comprehensive evaluation of the scaffold properties revealed that the incorporation of HA@SeNPs into the PLGA matrix did not compromise the mechanical performance of the scaffolds but significantly improved their degradation profile and biological functionality. Mechanical assessment under compression at 37 °C showed that the PLGA/HA@SeNPs composite scaffold exhibited a compressive modulus of 30 ± 1 MPa (Figure 4a). Mechanical evaluation after degradation showed that the scaffold retained 66.5% of its initial compressive modulus, indicating good retention of structural integrity (Figure 4b). This favorable mechanical performance was further supported by SEM analysis, which confirmed that the scaffold architecture remained well preserved, with characteristic surface erosion and an interconnected pore network that remained accessible for tissue ingrowth (Figure 4c).

The degradation behavior of the composite scaffolds was evaluated over an 8-week period. The scaffolds exhibited a controlled mass loss of 27.2% (Figure 4d). Notably, the incorporation of HA@SeNPs effectively buffered the acidic degradation by-products of PLGA, maintaining the pH of the degradation medium within the physiological range (7.1 ± 0.1), in marked contrast to the significant acidification (pH = 6.3 ± 0.3) observed in the pure PLGA scaffolds (Figure 4e).

Further characterization demonstrated enhanced surface bioactivity and physicochemical properties. After 14 days of immersion in simulated body fluid, the scaffold surfaces were densely covered with bone-like apatite crystals exhibiting a characteristic cauliflower-like morphology, demonstrating excellent biomineralization activity (Figure 4f). EDS point analysis of

Downloaded from academic.oup.com/burnstrauma/article/doi/10.1093/burnst/tkag049/8742059 by guest on 12 October 2026

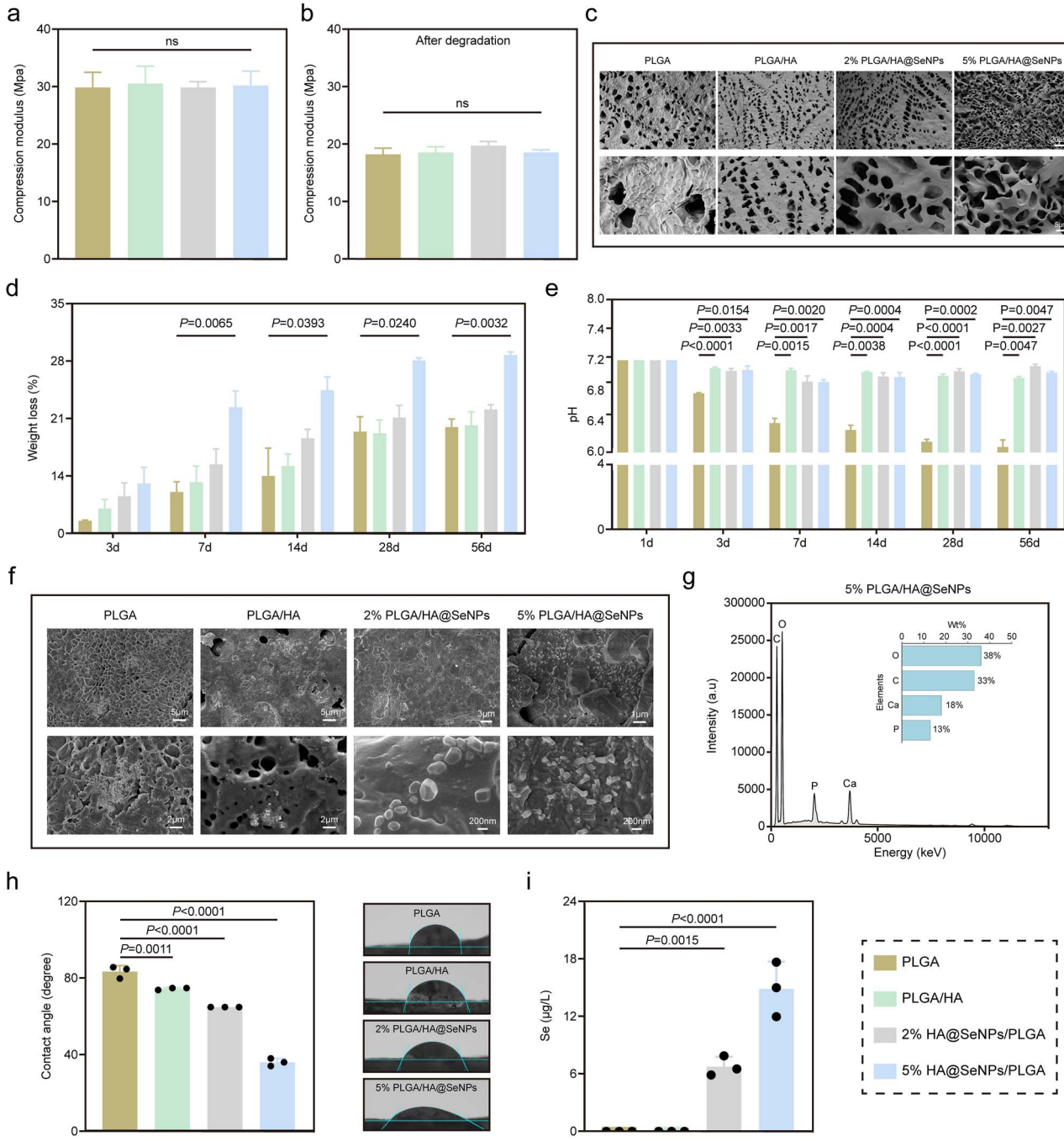


Figure 4 Mechanical properties, degradation behavior, and functional assessment of the PLGA/HA@SeNPs scaffolds. (**a**) Compressive modulus of the scaffolds. (**b**) Retention of compressive modulus after *in vitro* degradation. (**c**) SEM images showing the morphology of scaffolds post-degradation. Scale bar: 5 μm and 20 μm. (**d**) Mass loss of scaffolds after 8 weeks of degradation. (**e**) pH variation of the degradation medium over time. (**f**) SEM image of the scaffold surface after 14 days of immersion in simulated body fluid, showing mineralization. Scale bar: 1 μm, 2 μm, 3 μm, 5 μm and 200 μm. (**g**) EDS point analysis of the mineralized surface of the 5% HA@SeNPs/PLGA scaffold. (**h**) Water contact angle measurements on scaffold surfaces. (**i**) Cumulative Se release profile. Data are expressed as mean ± SD. *PLGA* poly(lactic-co-glycolic acid), *HA* hyaluronic acid, *SeNPs* selenium nanoparticles, *SEM* scanning electron microscopy, *EDS* energy-dispersive spectroscopy, *Se* selenium, *SD* standard deviation

the mineralized surfaces confirmed the formation of biological apatite, as evidenced by distinct calcium and phosphorus peaks. Compared with the pure PLGA group, the incorporation of HA@SeNPs promoted mineralization, yielding a calcium-to-phosphorus (Ca/P) ratio closer to that of natural bone apatite (Figure 4g and S1). This enhanced bioactivity was further supported by improved surface hydrophilicity, as evidenced by a reduction in the water contact angle from 84° ± 4° for pure PLGA to 36° ± 2° (Figure 4h). Finally, the scaffold exhibited a controlled Se release profile, with Se concentrations during the initial 72 h

Downloaded from academic.oup.com/burnstrauma/article/doi/10.1093/burnst/tkag049/8742059 by guest on 12 October 2026

remaining well within the safe therapeutic range of 0–20 μg/L (Figure 4i). Furthermore, the release study was extended to 56 days to evaluate long-term biosafety. At the end of the 56-day period, the Se concentration reached 65.41 $\pm$ 9.80 μg/L, which remained below the established safety threshold ($<$100 μg/L), indicating favorable long-term biocompatibility (Figure S2).

Based on the comprehensive evaluation of mechanical properties, degradation behavior, surface characteristics, bioactivity, and controlled release profile, the 5% PLGA/HA@SeNPs composite was selected for all subsequent biological experiments.

In vitro immunomodulatory performance and cellular responses

To optimize the HA@SeNPs concentration, the cytocompatibility of PLGA/HA@SeNPs scaffolds containing 1%, 2%, 5%, 8%, and 10% HA@SeNPs was evaluated using the CCK-8 assay. As shown in Figure S3, scaffolds containing 1%–5% HA@SeNPs exhibited excellent cell viability at days 1, 3, and 5, whereas concentrations exceeding 5% (8% and 10%) resulted in a significant decrease in viability ($P < 0.05$). Based on these results, together with the favorable printability and porosity, the 5% HA@SeNPs scaffold was selected for all subsequent experiments. The immunomodulatory potential of the PLGA/HA@SeNPs scaffolds was systematically evaluated in THP-1 macrophages. Live/dead staining and CCK-8 assays confirmed excellent cytocompatibility, with cell viability maintained above 95% throughout the 7-day culture period (Figure 5a–c). More importantly, the scaffolds demonstrated a marked capacity to direct macrophage polarization toward an anti-inflammatory M2 phenotype. RT-PCR analysis revealed a significant upregulation of M2 markers, including a 4.7-fold increase in IL-10 and 5.6-fold increase in Arg-1 expression compared with those in the control groups (Figure 5d). Conversely, M1 markers, such as iNOS and TNF-α, were substantially downregulated by 81% and 66%, respectively.

Western blot analysis provided further confirmation at the protein level, showing increased expression of the M2-associated proteins CD206 and Arg-1, whereas the expression of the M1-associated proteins iNOS and CD86 was significantly reduced (Figure 5e and f). Morphological evidence supporting this phenotypic shift was obtained by SEM, in which macrophages cultured on the scaffolds exhibited elongated, spindle-shaped morphologies characteristic of the M2 phenotype, in contrast to the rounded, amoeboid morphologies typical of the M1 phenotype. Notably, the SEM images also revealed intermediate morphologies indicative of a dynamic transition from the M1 to the M2 polarization state(Figure 5g). Immunofluorescence staining further demonstrated this phenotypic shift, with the scaffolds promoting the characteristic elongated M2 morphology and strong CD206 expression, in contrast to the rounded morphology and iNOS expression observed in the control group (Figure 6a, b and S4). The coordinated regulation of gene and protein expression confirmed the potent immunomodulatory capacity of the composite scaffold.

ELISA quantification of macrophage-secreted cytokines provided compelling evidence for the anti-inflammatory microenvironment created by the PLGA/HA@SeNPs composite scaffold. The cytokine secretion profiles demonstrated a significant reduction in the levels of the pro-inflammatory cytokines TNF-α and IL-6, which decreased by 34% and 46%, respectively, compared with the control group. Simultaneously, the production of the anti-inflammatory cytokines IL-10 and TGF-β1 increased significantly by 3.3-fold and 2.9-fold, respectively (Figure 6c).

Osteogenic differentiation potential and bone formation capacity

The osteoinductive capacity of the PLGA/HA@SeNPs composite scaffold was systematically evaluated using multiple analytical approaches. Functional assays provided direct evidence of enhanced osteogenic activity, with ALP staining showing significantly increased enzyme activity on day 7 (Figure 7a) and ARS staining revealing extensive mineralized nodule formation on day 21 (Figure 7b). This temporal progression from early osteogenic marker expression to mature matrix mineralization demonstrated the ability of the scaffold to support the complete osteogenic differentiation process. Immunofluorescence staining provided spatial visualization of this process, showing strong expression of the osteogenic markers osteopontin (OPN) and osteocalcin (OCN) in BMSCs cultured on the composite scaffold (Figure 7c and S5). Quantitative analysis confirmed that the fluorescence intensity of OPN and OCN was 1.4- and 1.7-fold higher, respectively, than those in in the control groups, indicating robust osteogenic commitment (Figure 7d). At the transcriptional level, RT-PCR analysis revealed a time-dependent upregulation of key osteogenic genes. After 7 days of culture, significant enhancements were observed in the expression of Runx2 (1.8-fold), Col1a1 (1.9-fold), ALP (1.5-fold), Ibsp (1.5-fold), and OPN (1.3-fold) compared with those in controls (Figure 7e and S6).

Building on insights from our previous experimental results, we performed transcriptomic profiling to further elucidate the molecular mechanisms by which the PLGA/HA@SeNPs scaffold enhances osteogenic differentiation. Bulk RNA sequencing analysis after culturing BMSCs with the scaffold revealed significant differential gene expression, with 857 upregulated and 954 downregulated genes, as illustrated in the volcano plot and heatmap (Figure 8a and b). KEGG pathway enrichment analysis of these differentially expressed genes highlighted pronounced activation of the mitogen-activated protein kinase (MAPK) signaling pathway. GSEA further confirmed the robust enrichment of MAPK-related gene sets in the scaffold-treated group (Figure 8c and d). Consistent with the transcriptional profile, western blot analysis demonstrated elevated protein levels of key MAPK pathway components, including ERK, phosphorylated MAPK (p-MAPK), and total MAPK, in cells cultured with the PLGA/HA@SeNPs scaffold compared with controls. To functionally validate the involvement of the MAPK pathway, a PLGA/HA@SeNPs + U0126 group was added and compared with the control and PLGA/HA@SeNPs groups. Western blot analysis confirmed that U0126 treatment effectively reduced the phosphorylation levels of MAPK, p-MAPK, and ERK1/2, indicating successful pathway inhibition (Figure 8e and f). Immunofluorescence staining further showed that the PLGA/HA@SeNPs scaffold significantly upregulated ERK expression, while U0126 treatment suppressed this upregulation (Figure 8g and h). Collectively, these data provide direct functional evidence that the PLGA/HA@SeNPs

Downloaded from academic.oup.com/burnstrauma/article/doi/10.1093/burnst/tkag049/8742059 by guest on 12 October 2026

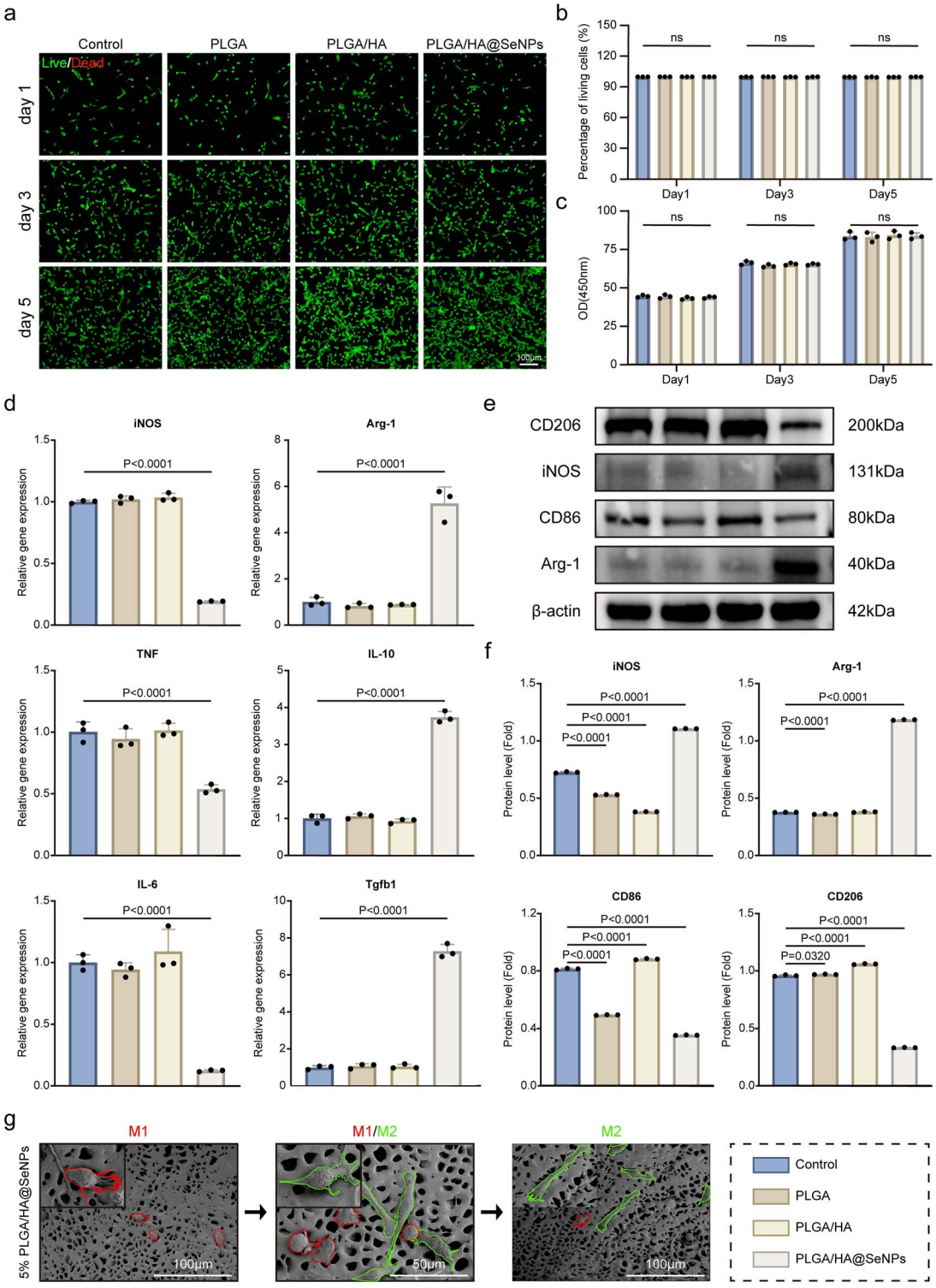


Figure 5 *In vitro* immunomodulatory effects of PLGA/HA@SeNPs scaffolds on THP-1 macrophages. (**a**) Live/dead fluorescence staining images of macrophages cultured on scaffolds. Scale bar: 100 μm. (**b**) Quantitative analysis of cell viability from live/dead staining. (**c**) Cell viability assessed by CCK-8 assay. (**d**) Relative mRNA expression levels of M1 markers (iNOS, TNF-α, IL-6) and M2 markers (Arg-1, IL-10, TGF-β1) measured by RT-PCR. (**e**) Representative Western blot bands of M1/M2-associated proteins (iNOS, CD86, Arg-1, CD206). (**f**) Quantitative analysis of the protein expression levels. (**g**) SEM images illustrating the morphological transition of macrophages from a rounded (M1-like) to an elongated (M2-like) phenotype on the scaffolds. Scale bar: 50 μm and 100 μm. Data are expressed as mean $\pm$ SD. For time-course data in (b) and (c), two-way ANOVA with Tukey's post-hoc test was applied, considering all samples as independent. *PLGA* poly(lactic-co-glycolic acid), *HA* hyaluronic acid, *SeNPs* selenium nanoparticles, *THP-1* human monocytic cell line, *CCK-8* cell counting kit-8, *iNOS* inducible nitric oxide synthase, *TNF-α* tumor necrosis factor-alpha, *Arg-1* arginase-1, *IL* interleukin, *RT-PCR* reverse transcription polymerase chain reaction, *SEM* scanning electron microscopy, *SD* standard deviation, *ANOVA* analysis of variance

Downloaded from academic.oup.com/burnstrauma/article/doi/10.1093/burnst/tkag049/8742059 by guest on 12 October 2026

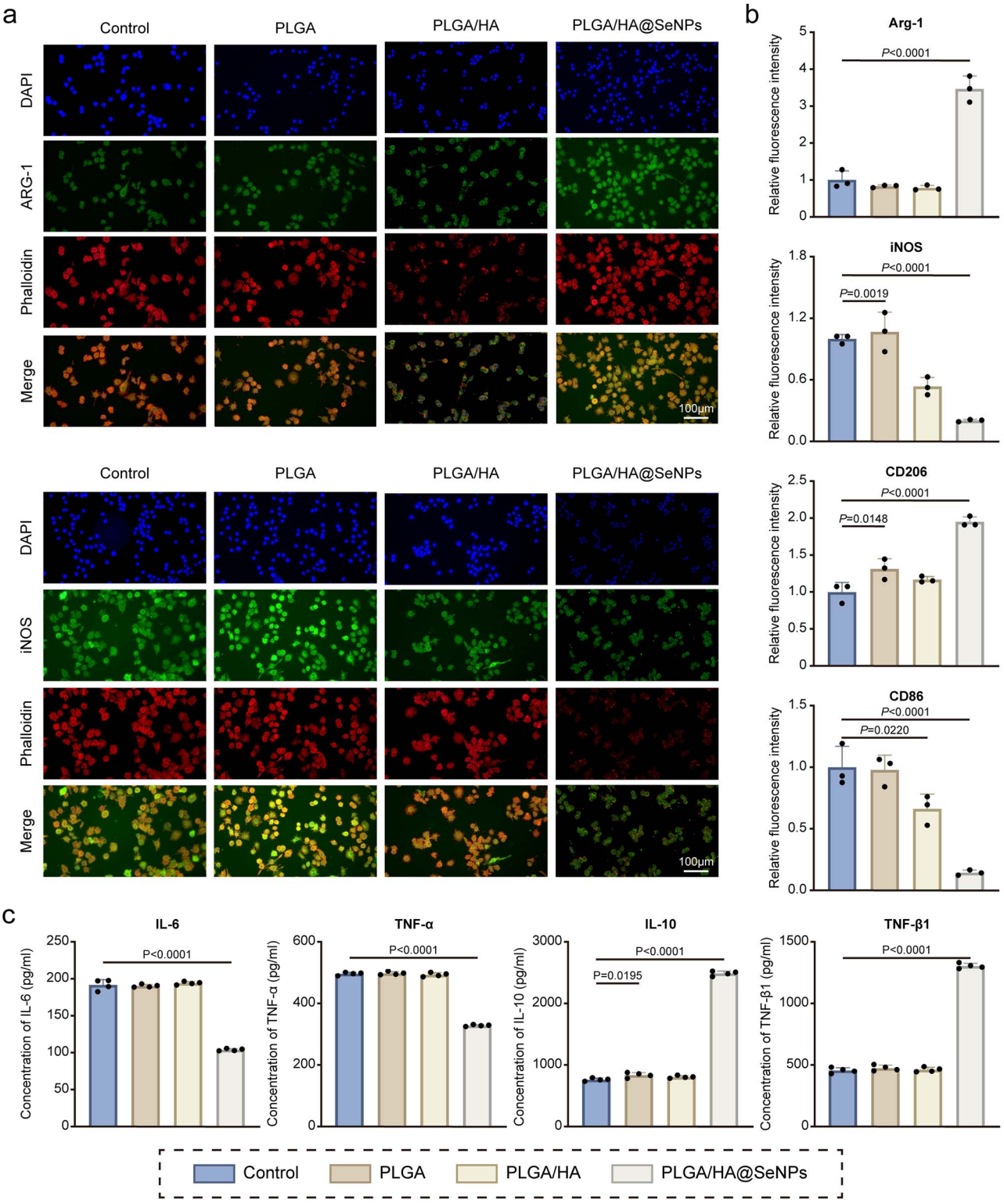


Figure 6 Immunofluorescence analysis and cytokine secretion profile of macrophages. (**a**) Immunofluorescence staining for the M2 marker CD206 (green). Scale bar: 100 μm. (**b**) Immunofluorescence staining for the M1 marker iNOS (green). (**c**) Concentrations of secreted cytokines (TNF-α, IL-6, IL-10, TGF-β1) in the culture supernatant, quantified by ELISA. Data are expressed as mean $\pm$ SD. *iNOS* inducible nitric oxide synthase, *TNF-α* tumor necrosis factor-alpha, *IL* interleukin, *TGF-β1* transforming growth factor-beta 1, *ELISA* enzyme-linked immunosorbent assay, *SD* standard deviation

Downloaded from academic.oup.com/burnstrauma/article/doi/10.1093/burnst/tkag049/8742059 by guest on 12 October 2026

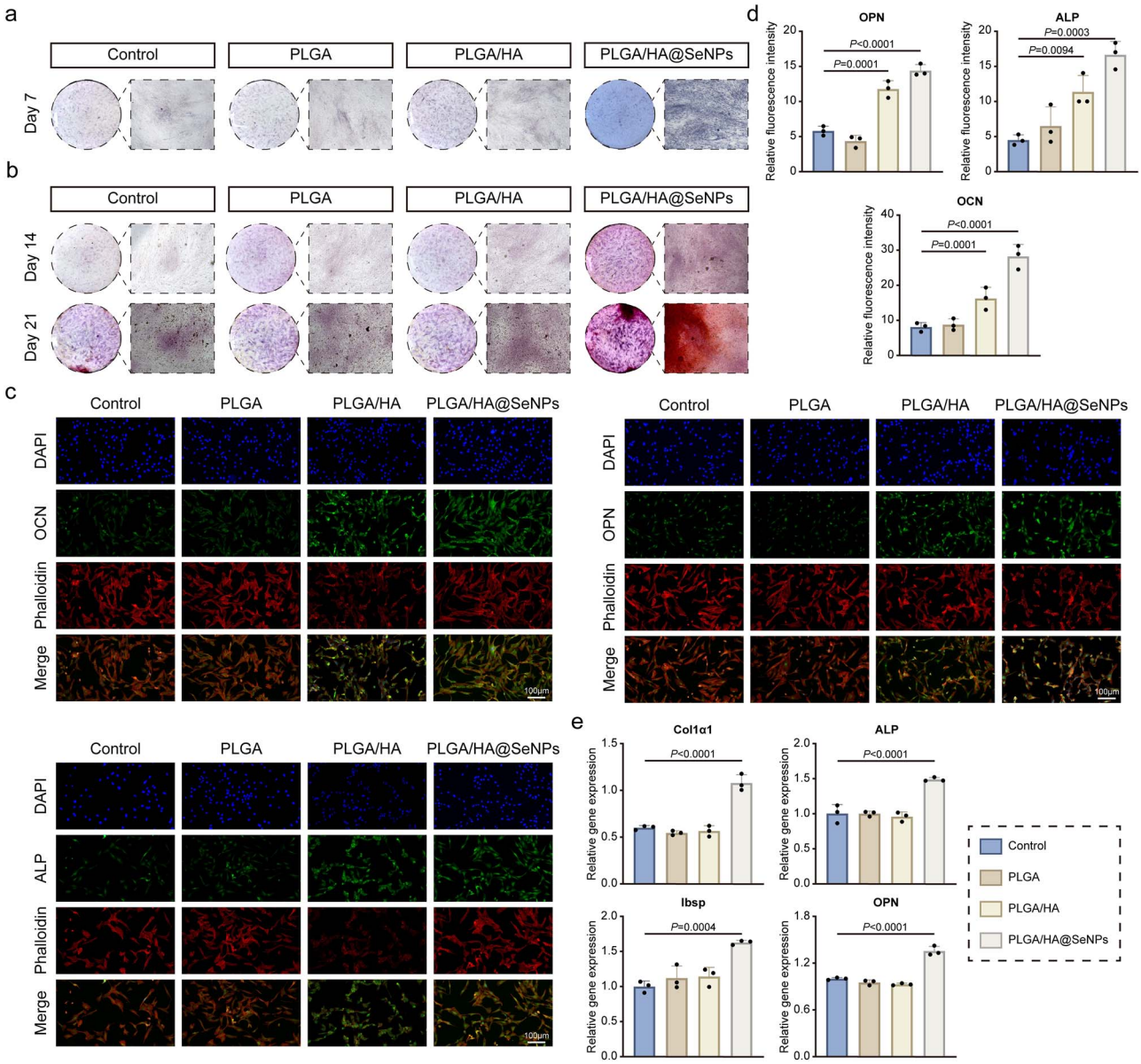


Figure 7 Osteogenic differentiation of BMSCs cultured on PLGA/HA@SeNPs scaffolds. (**a**) ALP staining on day 7. (**b**) ARS staining on days 14 and 21. (**c**) Immunofluorescence staining for osteogenic markers OCN, OPN, and ALP. Scale bar: 100 μm. (**d**) Quantitative analysis of the immunofluorescence intensity for OCN, OPN, and ALP. (**e**) Relative mRNA expression levels of osteogenic genes (Col1a1, ALP, Ibsp, OPN) measured by RT-PCR. Data are expressed as mean $\pm$ SD. For time-dependent gene expression data in (e), two-way ANOVA with Tukey's post-hoc test was used, with time and scaffold composition as independent factors. *BMSCs* bone marrow mesenchymal stem cell, *PLGA* poly(lactic-co-glycolic acid), *HA* hyaluronic acid, *SeNPs* selenium nanoparticles, *ALP* alkaline phosphatase, *ARS* alizarin red S, *Runx2* runt-related transcription factor 2, *OCN* osteocalcin, *OPN* osteopontin, *RT-PCR* reverse transcription polymerase chain reaction, *SD* standard deviation, *ANOVA* analysis of variance, *Ibsp* integrin-binding sialoprotein, *Col1a1* collagen type I alpha 1

scaffold promotes osteogenesis at least partially through activation of the MAPK signaling pathway. Collectively, these data suggest that the PLGA/HA@SeNPs scaffold may promote osteogenesis through activation of the MAPK signaling pathway.

Together, these results demonstrate that the PLGA/HA@SeNPs scaffold promotes osteogenic differentiation and matrix mineralization through a synergistic combination of its hierarchical microstructure and sustained release of bioactive selenium. The consistent enhancement observed across functional assays, protein localization, and gene expression confirms the scaffold's potent osteoinductive capability, underscoring its potential as an integrated platform for bone regeneration.

In vivo bone regeneration efficacy and host integration

Micro-computed tomography quantification of bone defect repair

The bone-regenerative efficacy of the PLGA/HA@SeNPs scaffolds was evaluated in a critically sized rat femoral defect model, as schematically (Figure 9a). Micro-CT analysis performed at 6 and 12 weeks post-implantation revealed that, by the final 12-week time point, substantial bone regeneration had occurred in the scaffold group, achieving a bone volume fraction (BV/TV) of 56% $\pm$ 1%. This was significantly higher than that in the PLGA-only

Downloaded from academic.oup.com/burnstrauma/article/doi/10.1093/burnst/tkag049/8742059 by guest on 12 October 2026

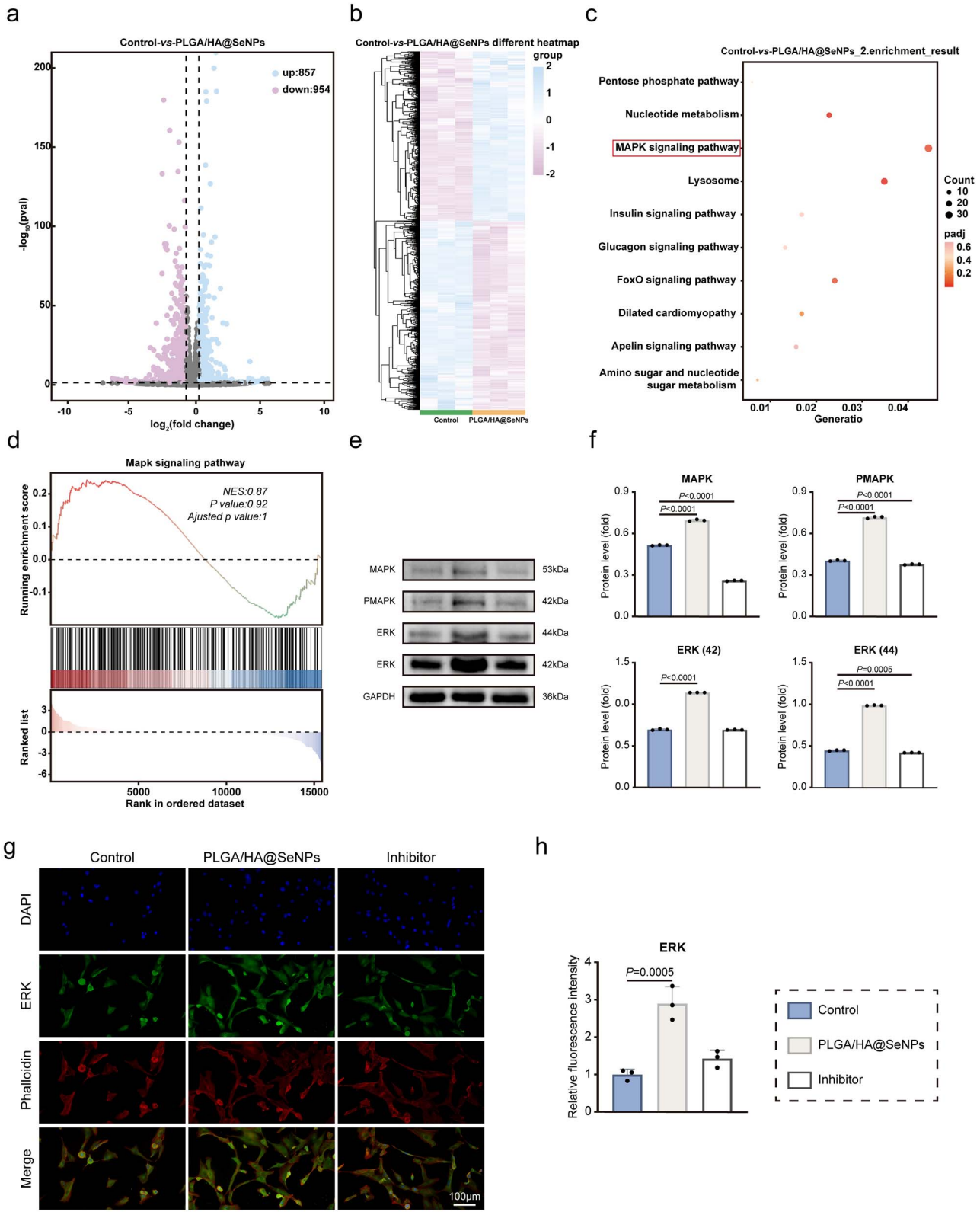


Figure 8 Transcriptomic profiling and mechanistic exploration of the osteogenic effects mediated by the PLGA/HA@SeNPs scaffold. (**a**) Volcano plot illustrating differentially expressed genes. (**b**) Heatmap of gene expression patterns. (**c**) KEGG showing enriched pathways in scaffold-treated cells. (**d**) GSEA enrichment plot for the MAPK signaling pathway. (**e**) Western blot analysis of key MAPK pathway proteins in control and PLGA/HA@SeNPs groups. (**f**) Quantitative analysis of protein expression levels. (**g**) Immunofluorescence staining of ERK. Scale bar: 100 μm. (**h**) Quantitative analysis of relative fluorescence intensity. Data are expressed as mean ± SD. *PLGA* poly(lactic-co-glycolic acid), *HA* hyaluronic acid, *SeNPs* selenium nanoparticles, *KEGG* kyoto encyclopedia of genes and genomes, *GSEA* gene set enrichment analysis, *MAPK* mitogen-activated protein kinase, *ERK* extracellular signal-regulated kinase, *SD* standard deviation

Downloaded from academic.oup.com/burnstrauma/article/doi/10.1093/burnst/tkag049/8742059 by guest on 12 October 2026

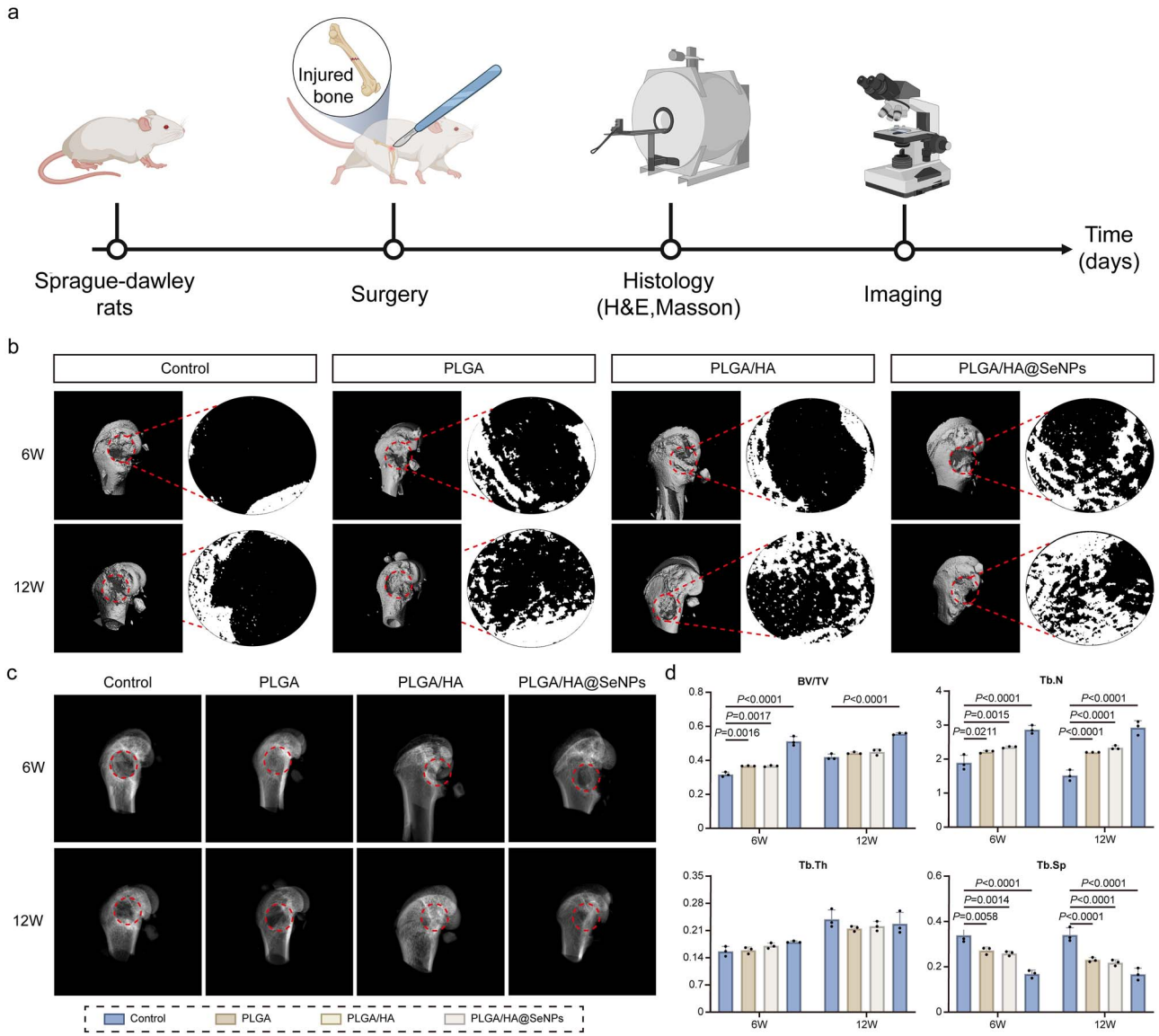


Figure 9 *In vivo* bone regeneration evaluated in a rat femoral defect model. (**a**) Schematic illustration of the critical-sized femoral defect model and scaffold implantation. (**b**) 3D reconstructions from micro-CT scans, showing NB formation and defect bridging at 6 and 12 weeks. (**c**) Representative 2D micro-CT cross-sectional images of the defect sites at 6 and 12 weeks post-implantation. (**d**) Quantitative analysis of bone regeneration parameters: BV/TV, Tb.Th, Tb.N, and Tb.Sp, presented as bar graphs at 6 and 12 weeks. Data are expressed as mean ± SD. Data in (d) were analyzed by two-way ANOVA followed by Tukey's post-hoc test, with all samples treated as independent. *micro-CT* micro-computed tomography, *NB* new bone, *BV/TV* bone volume/total volume, *Tb.Th* trabecular thickness, *Tb.N* trabecular number, *SD* standard deviation, *ANOVA* analysis of variance, *Tb.Sp* trabecular separation

(46% ± 3%) and empty defect (42% ± 2%) groups (Figure 9b–d). Three-dimensional reconstruction demonstrated complete defect bridging and seamless integration with the native bone tissue at 12 weeks. Quantitative analysis showed well-organized trabecular architecture with optimized structural parameters, including trabecular thickness (Tb.Th) of 0.22 ± 0.04 mm and Tb.N of 2.6 ± 0.5 mm^{-1}. These *in vivo* findings collectively demonstrate that the PLGA/HA@SeNPs scaffold possesses significantly better bone-repair efficacy than the pure PLGA scaffold, which is consistent with the osteogenic enhancement observed *in vitro*.

Histological evaluation of new bone formation and scaffold integration

Histological examination provided a detailed characterization of the regeneration process and host response. H&E staining revealed that the PLGA/HA@SeNPs scaffold group exhibited minimal inflammatory cell infiltration, indicating favorable biocompatibility and an attenuated early immune response. Concurrently, extensive new bone formation was observed, with abundant osteoblasts actively depositing osteoid matrix throughout the defect area (Figure 10a). Masson's trichrome staining further demonstrated mature, yet appropriately organized, collagen matrix deposition at the defect site, with excellent integration between the regenerated bone and the host tissue (Figure 10b). The scaffold exhibited progressive degradation synchronized with new bone formation, and direct bone-scaffold contact was observed without fibrous tissue interposition, indicating excellent osseointegration.

Immunofluorescence double labeling of osteogenic and inflammatory markers revealed that the PLGA/HA@SeNPs scaffold

Downloaded from academic.oup.com/burnstrauma/article/doi/10.1093/burnst/tkag049/8742059 by guest on 12 October 2026

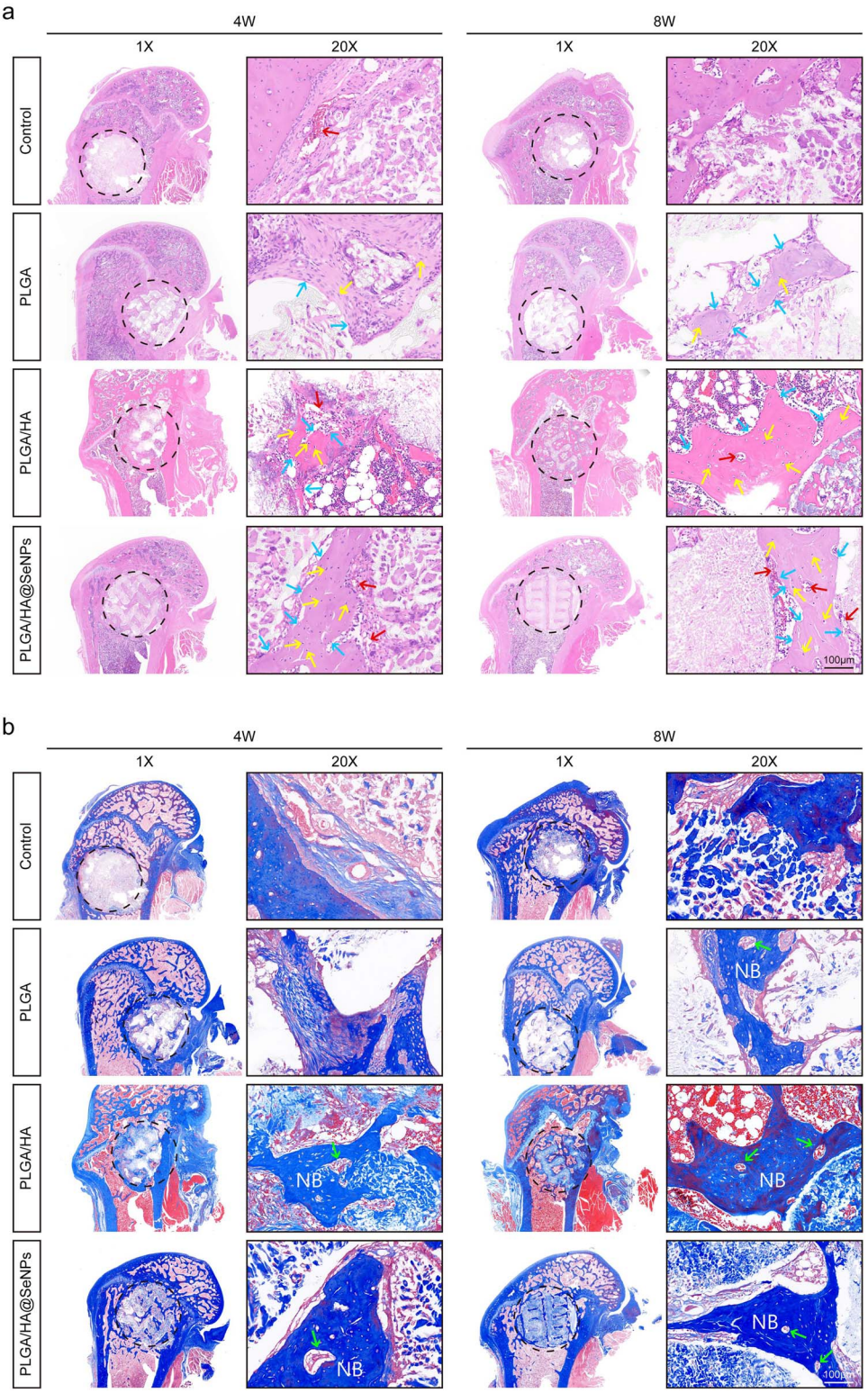


Figure 10 Histological evaluation of NB formation and host integration in the rat femoral defect model. (**a**) Representative H&E staining images of the defect areas at 12 weeks post-implantation. The original defect boundary is outlined with a black dashed line. Red arrows indicate nascent vasculature, yellow arrows indicate osteocytes, and blue arrows point to active osteoblasts lining the osteoid surfaces. Scale bar: 1000 μm. (**b**) Representative Masson's trichrome staining images of the defect areas at 12 weeks. The defect boundary is similarly demarcated by a black dashed line. Green arrows denote regenerated blood vessels, and areas of prominent NB formation are labeled as "NB". Scale bar: 100 μm & 1000 μm. Data are expressed as mean $\pm$ SD. *NB* new bone, *H&E* hematoxylin and eosin, *SD* standard deviation

Downloaded from academic.oup.com/burnstrauma/article/doi/10.1093/burnst/tkag049/8742059 by guest on 12 October 2026

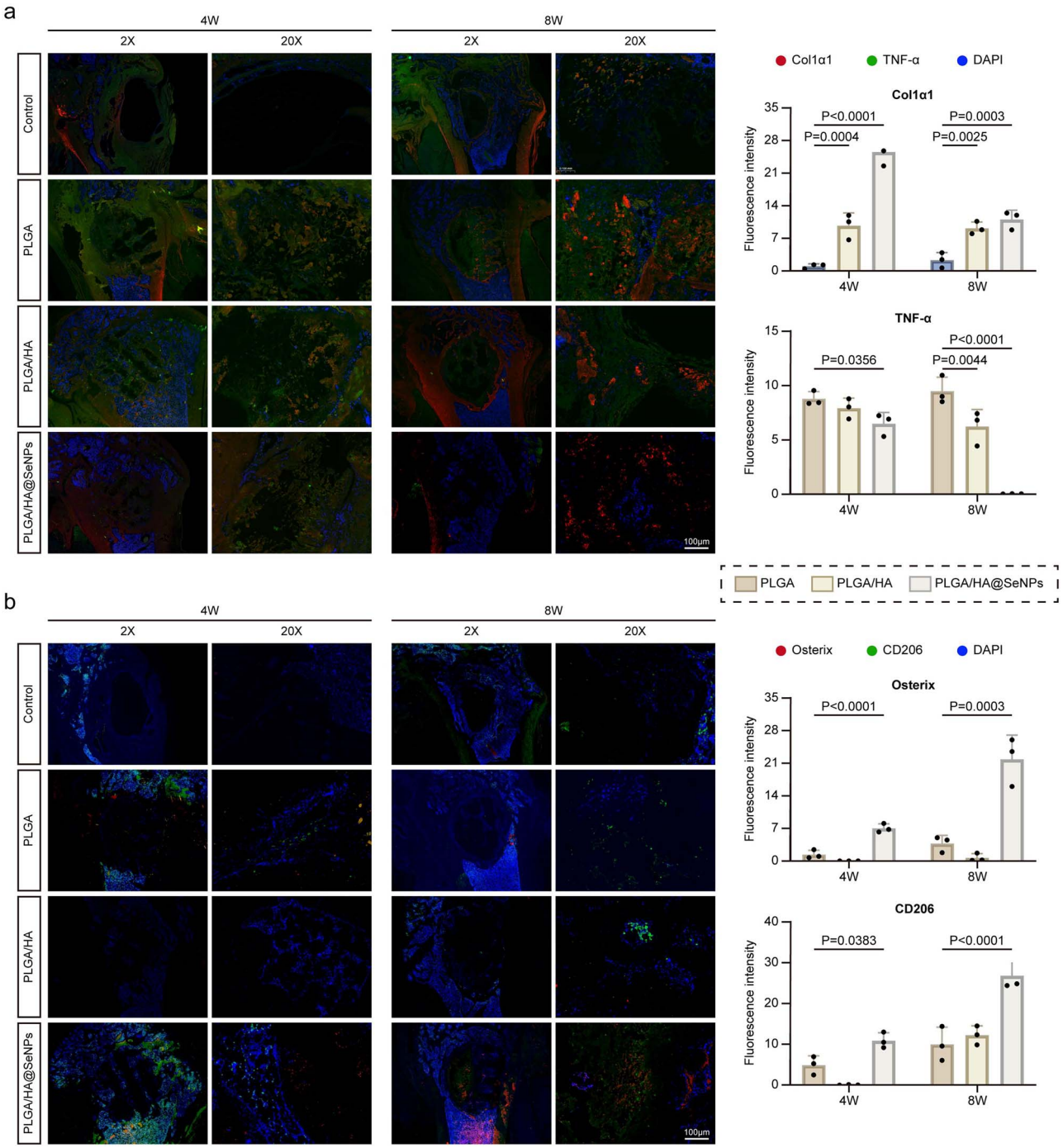


Figure 11 *In vivo* immunofluorescence evaluation of osteogenic and immunomodulatory responses in critical-sized femoral defects. (**a**) Representative immunofluorescence images of Col1α1 (red) and TNF-α (green) co-staining, along with quantitative analysis of fluorescence intensity across control, PLGA, and PLGA/HA@SeNPs groups. Scale bar: 100 μm. (**b**) Immunofluorescence images of OSX (red) and CD206 (green) co-staining, with corresponding quantitative analysis of signal intensity in the three experimental groups. Scale bar: 100 μm. Data are expressed as mean $\pm$ SD. *TNF-α* tumor necrosis factor-alpha, *PLGA* poly(lactic-co-glycolic acid), *HA* hyaluronic acid, *SeNPs* selenium nanoparticles, *OSX* osterix, *SD* standard deviation

effectively mitigated inflammation while promoting osteogenesis in vivo, in contrast to the PLGA control group. For Col1α1/TNF-α staining, a distinct spatial segregation was observed (Figure 11a). Strong Col1α1 fluorescence, indicative of active bone matrix synthesis, was localized primarily to osteoblasts and newly formed bone matrix in the PLGA/HA@SeNPs group. In contrast, the TNF-α signal, a marker of pro-inflammatory M1 macrophages, was markedly attenuated in these osteogenic regions. Conversely, areas with residual TNF-α+ cell infiltration exhibited minimal Col1α1 expression. This reciprocal distribution suggests an inhibitory relationship between inflammation and bone formation. Double labeling of OSX and CD206 further elucidated the immunomodulatory osteogenic microenvironment (Figure 11b). *In the PLGA/HA@SeNPs group, OSX+ osteoprogenitor cells were abundantly present at the bone formation front. Notably, these regions were frequently populated by CD206+ cells, representing*

Downloaded from academic.oup.com/burnstrauma/article/doi/10.1093/burnst/tkag049/8742059 by guest on 12 October 2026

pro-healing M2 macrophages. A clear spatial association and partial colocalization between OSX+ and CD206+ cells were evident, suggesting synergistic crosstalk. Overall, the histological evidence demonstrates that the PLGA/HA@SeNPs scaffold supports more advanced bone repair than the pure PLGA scaffold, as reflected by enhanced osteogenesis, immunomodulation, and scaffold-bone integration. These in vivo observations are consistent with the immunomodulatory and osteogenic enhancements demonstrated in vitro.

To further evaluate the *in vivo* safety of the PLGA/HA@SeNPs scaffold, major organs (heart, liver, spleen, lungs, and kidneys) were harvested from each animal at the 12-week endpoint and subjected to H&E staining. As shown in Figure S7, histological examination revealed normal tissue architecture in all organ sections, without evidence of necrosis, pathological lesions, or abnormal inflammatory cell infiltration in any treatment group compared with the blank control. These findings indicate that the PLGA/HA@SeNPs scaffold and its degradation products do not cause detectable organ toxicity, supporting their favorable long-term biocompatibility and potential for further translational development.

Discussion

The paradigm of bone regeneration is shifting from the passive provision of structural support to the active orchestration of the immune microenvironment, which plays a critical role in the healing of complex bone defects [49]. The paradigm of bone regeneration is shifting from the passive provision of structural support to the active orchestration of the immune microenvironment, which plays a critical role in the healing of complex bone defects [50]. Consistent with this paradigm, the development of immunomodulatory metal-based biomaterials (e.g., biodegradable zinc alloys) has gained considerable attention. Accordingly, we developed a multifunctional PLGA/HA@SeNPs scaffold [51]. In this context, several studies have reported the use of SeNPs or PLGA-based nanocomposites for immunomodulation and bone repair. However, most of these studies have either focused on a single aspect (e.g., antioxidant effects) or lacked systematic in vivo validation. In the present study, we developed a PLGA/HA@SeNPs scaffold that integrates multiple functional features into a single platform. Its primary innovation lies in creating a synergistic microenvironment in which the intrinsic hierarchical microstructure of the scaffold provides physical cues to cells, whereas the HA@SeNPs complex delivers sustained biochemical stimulation, collectively promoting bone regeneration through a material-based, drug-free strategy. Fabricated *via* cryogenic 3D bioprinting, this platform uniquely enables the precise spatial patterning of the immunomodulatory HA@SeNPs within the mechanically robust PLGA matrix, while simultaneously constructing a hierarchically interconnected porous network (macropores of 150–300 μm and micropores of 1–5 μm) that closely mimics the native bone extracellular matrix. Although cryogenic 3D printing is an established technique for preserving bioactivity, its combination with HA@SeNPs in a single scaffold for osteo-immunomodulation has not been previously reported. In contrast, conventional scaffolds, such as those composed of PLGA or hydroxyapatite alone, lack this targeted, active immune-instructive capability, often rendering them inadequate for overcoming the hostile immune microenvironment in critical-sized bone defects, thereby limiting their biointegration and regenerative efficacy [52–54].

The distinctive advantage of this scaffold lies in its dual functionality: it serves as a structurally competent template while actively interacting with and modulating the local immune system. The key outcome is the reprogramming of the local immune microenvironment from a pro-inflammatory to a pro-regenerative state. This shift is fundamental to bone healing because a prolonged inflammatory phase is a well-recognized barrier to successful regeneration [55, 56]. The ability of the scaffold to attenuate inflammation and promote an anti-inflammatory microenvironment is therefore crucial for initiating the subsequent stages of healing. Moreover, the sustained activity of the HA@SeNPs complex ensures that this immunomodulatory effect is not transient but is maintained throughout the critical early and intermediate phases of repair. Structurally, the mechanical properties of the scaffold are integrated with its bioinstructive function [57]. The similarity of its compressive modulus to that of cancellous bone suggests that it can protect the defect from detrimental mechanical forces while facilitating beneficial mechanotransduction. The degradation kinetics, characterized by surface erosion, act in concert with ionic release to progressively create space for new tissue ingrowth while continuously providing biochemical cues that promote osteoblast function and mitigate oxidative stress. This dynamic interplay between structural support and active immunomodulation positions the scaffold as a temporary yet instructive regulator of the healing process.

Furthermore, the scaffold exerted direct and potent osteogenic effects by creating a highly conducive environment for bone formation. Following its initial immunomodulatory role, the HA component facilitated the adhesion and proliferation of osteoprogenitor cells, such as BMSCs, thereby creating a favorable substrate for early osteogenic events. SeNPs, acting synergistically with the HA matrix, significantly accelerated the osteogenic differentiation process. This finding aligns with the growing emphasis on nanoparticle-based strategies for promoting bone healing [13, 58]. Furthermore, emerging evidence indicates that selenium nanoparticles may also regulate programmed cell death pathways such as ferroptosis and pyroptosis, which are increasingly recognized as key contributors to the osteo-immune microenvironment [59]. This was evidenced by the marked upregulation of early and late osteogenic markers, enhanced ALP activity, and robust matrix mineralization, demonstrating the intrinsic capacity of the scaffold to initiate the osteogenic program. Consistent with our in vitro mechanistic findings, a plausible explanation for the observed in vivo bone healing is that the scaffold provides a protective microenvironment that is crucial for osteogenesis at challenging defect sites. By effectively scavenging ROS, SeNPs protect osteoprogenitor cells and osteoblasts from oxidative stress-induced apoptosis and functional impairment. This preserves the viability and anabolic activity of bone-forming cells, which are indispensable for successful regeneration [60–62]. Collectively, these in vitro and in vivo findings suggest that the PLGA/HA@SeNPs system functions as an active osteoinductive construct that not only promotes the commitment of progenitor cells to the osteoblastic lineage but also supports bone matrix deposition and mineralization, thereby providing a mechanistic basis for the observed de novo bone formation in critical-size defects.

Downloaded from academic.oup.com/burnstrauma/article/doi/10.1093/burnst/tkag049/8742059 by guest on 12 October 2026

We acknowledge that the present study did not include direct comparisons with other well-established immunomodulatory strategies (e.g. those based on exogenous cytokines, exosomes, or alternative metal ions), which limits the contextualization of the relative performance of our platform [63]. Nonetheless, the drug-free, Se-based design of the scaffold offers potential advantages in terms of cost, stability, and regulatory simplicity. Despite these promising features, the present study has several limitations that warrant consideration. Mechanistic insights derived primarily from human THP-1 cell models and rodent calvarial defect studies may not fully capture the complex osteoimmune interactions within large load-bearing bones or compromised physiological states [64, 65]. Moreover, several translational hurdles remain to be addressed. First, although no obvious cytotoxicity was observed in the heart, liver, lung, or kidney tissues after scaffold implantation and sustained Se release remained below the safety threshold ($<100\ \mu g/L$) over 56 days, long-term systemic biosafety, particularly the biodistribution and potential accumulation of Se in metabolic organs over extended periods, still requires thorough investigation [66–68]. Furthermore, the clearance pathways and potential long-term effects of PLGA/HA@SeNPs degradation products (lactic acid, glycolic acid, HA fragments, and Se species) in clinical settings need to be characterized in future studies. In addition, the speciation of the released Se (e.g., whether it remains as elemental Se^0 or is oxidized to selenite or selenate) was not analyzed in this study, limiting the understanding of its precise bioactivity and long-term toxicity. To address these limitations, future research will include large-animal models with critical-size, load-bearing defects to rigorously evaluate the clinical translational potential of the scaffold. Future studies will also integrate longitudinal analyses of degradation kinetics with multi-omics approaches (e.g., transcriptomics and proteomics) to elucidate the precise molecular mechanisms through which SeNPs mediate osteoimmune crosstalk. Ultimately, coupling this scaffold platform with patient-specific immunophenotyping could contribute to personalized bone regeneration strategies, particularly for challenging clinical conditions such as osteoporosis and diabetes.

In summary, this study demonstrates that the cryogenic 3D-printed PLGA/HA@SeNPs scaffold can effectively regulate macrophage polarization and enhance bone regeneration in a critical-sized femoral defect model through the cooperative contributions of its hierarchical microtopography, HA-mediated adhesion, and selenium-based immunomodulation. This integrated strategy offers a promising therapeutic approach for critical-sized bone defects and may inform the design of future immunomodulatory biomaterials.

Conclusions

This study successfully established a novel osteoimmunomodulatory strategy through the development of a cryogenic 3D-printed PLGA/HA@SeNPs scaffold fabricated by cryogenic 3D bioprinting. The distinctive hierarchical microstructure of the scaffold, combined with the immunomodulatory functionality of the HA@SeNPs complex, created a multifunctional platform that simultaneously addressed immune microenvironment regulation and bone regeneration. The HA@SeNPs complex effectively promoted macrophage polarization toward the M2 phenotype, potentially through the redox-regulating properties of Se, while directly enhancing the osteogenic differentiation of mesenchymal stem cells. Importantly, the optimized mechanical properties and controlled degradation profile of the scaffold ensured that structural support was synchronized with new bone formation. Both in vitro and in vivo evaluations consistently demonstrated the superior capacity of the scaffold to modulate immune responses and accelerate bone repair in critical-size bone defects. These findings not only validate the PLGA/HA@SeNPs composite scaffold as an effective bone graft substitute but also highlight the importance of incorporating multifunctional immunomodulatory components into biomaterial design for advanced tissue engineering applications.

Abbreviations

ALP, alkaline phosphatase; ARS, Alizarin red staining; BMSC, bone marrow mesenchymal stem cell; BV/TV, bone volume/total volume; DMEM, Dulbecco's modified Eagle's medium; EDS, energy-dispersive X-ray spectroscopy; FBS, fetal bovine serum; FTIR, Fourier transform infrared spectroscopy; HA, hyaluronic acid; hBMSC, human bone marrow mesenchymal stem cell; HRTEM, high-resolution transmission electron microscopy; PBS, phosphate-buffered saline; PLGA, poly(lactic-co-glycolic acid); Se, selenium; SEM, scanning electron microscopy; SeNPs, selenium nanoparticle; Tb.N, trabecular number; Tb.Sp, trabecular separation; Tb.Th, trabecular thickness; TBST, Tris-buffered saline; TEM, transmission electron microscopy; XRD, X-ray diffraction; XPS, X-ray photoelectron spectroscopy.

Author contributions

Shengwen Cheng (Conceptualization [lead], Data curation [lead], Formal analysis [lead], Investigation [lead], Methodology [lead], Project administration [lead], Writing—original draft [lead]), Yuqiao Wang (Data curation [equal], Formal analysis [equal], Investigation [equal], Methodology [equal], Project administration [equal], Writing—original draft [equal]), Yu Zhai (Investigation [equal], Methodology [equal], Project administration [equal], Writing—original draft [equal]), Mingfei Dong (Investigation [equal], Methodology [equal], Project administration [equal]), Xiaole Peng (Methodology [equal], Project administration [equal]), Xiaohong Luo (Methodology [equal], Project administration [equal]), Jiacheng Liu (Methodology [equal], Project administration [equal]), Junyan Liu (Methodology [equal], Project administration [equal]), Yi He (Investigation [equal], Methodology [equal]), Xiaoxiong Li (Methodology [equal], Project administration [equal]), Ke Huang (Methodology [equal], Project administration [equal]), Senrui Liu (Methodology [equal], Project administration [equal]), Fengyuan Liu (Supervision [equal], Writing—review & editing [equal]), Yuwei Zhang (Methodology [equal]), Zhong Alan Li (Supervision [equal], Writing—review & editing [equal]), Wei Huang (Funding acquisition [equal], Supervision [equal], Validation [equal], Visualization [equal], Writing—review & editing [equal]), Chen Zhao (Conceptualization [equal], Funding acquisition [equal], Supervision [equal], Validation [equal], Visualization [equal], Writing—review & editing [equal]), and Yiting Lei (Conceptualization [lead], Funding acquisition

Downloaded from academic.oup.com/burnstrauma/article/doi/10.1093/burnst/tkag049/8742059 by guest on 12 October 2026

[lead], Supervision [lead], Validation [lead], Visualization [lead], Writing—review & editing [lead])

Supplementary material

Supplementary material is available at *Burns & Trauma* online.

Ethics approval and consent to participate

Animal models were established using standard protocols approved by the Experimental Animal Management and Use Committee of Chongqing Medical University (IACUC-CQMU; Approval No. IACUC-CQMU-2024-0382).

Conflicts of interest

None declared.

Funding

This work was supported by the National Natural Science Foundation of China (82302755, U22A20284, 82202724), Scientific and Technological Research Project of Chongqing Municipal Education Commission (KJQN202400436), Hong Kong Scholars Program (XJ2024017), Natural Science Foundation of Chongqing, China (CSTB2024NSCQ-MSX1200, CSTB2024NSCQ-MSX1226), Science and Technology Research Project of Chongqing Education Commission (XJQN202200474), China Postdoctoral Science Foundation (2024MD754037), and Sichuan Science and Technology Program (23NSFSC5880).

Data availability

Data are available from the corresponding author upon reasonable request.

References

1. Hao S, Wang M, Yin Z, Jing Y, Bai L, Su J. Microenvironment-targeted strategy steers advanced bone regeneration. *Mater Today Bio.* 2023;22:100741. https://doi.org/10.1016/j.mtbio.2023.100741
2. Jin Y, Huang Y, Wang J, Zhou X, Chen J, Ding W, *et al.* From injury to integrity: tissue engineering solutions in combined bone repair and regeneration and muscle repair. *Burns Trauma.* 2025;13:tkaf052. https://doi.org/10.1093/burnst/tkaf052
3. Chen L, Ai Y, Wu R, Guo Z, Li Y, Li J, *et al.* Cationized decalcified bone matrix for infected bone defect treatment. *BME Frontiers.* 2024;5:0066. https://doi.org/10.34133/bmef.0066
4. Cheng S, Zhao C, Liu S, Chen B, Chen H, Luo X, *et al.* Injectable self-setting ternary calcium-based bone cement promotes bone repair. *ACS Omega.* 2023;8:16809–23. https://doi.org/10.1021/acsomega.3c00331
5. Łuczak JW, Palusińska M, Matak D, Pietrzak D, Nakielski P, Lewicki S, *et al.* The future of bone repair: emerging technologies and biomaterials in bone regeneration. *Int J Mol Sci.* 2024;25:12766. https://doi.org/10.3390/ijms252312766.
6. Lv Z, Ji Y, Wen G, Liang X, Zhang K, Zhang W. Structure-optimized and microenvironment-inspired nanocomposite biomaterials in bone tissue engineering. *Burns Trauma.* 2024;12:tkae036. https://doi.org/10.1093/burnst/tkae036
7. Gu A, Lao A, Li W, Liu Z, Zhou C, Cai J, *et al.* Prussian blue nanoparticles promoting diabetic bone regeneration via mitochondrial recovery. *BME Frontiers.* 2025;6:0204. https://doi.org/10.34133/bmef.0204
8. Zhang H, Wang J, Yang R, Song X, Liu R, Wang J, *et al.* A native bioactive Interface functionalized with osteoprogenitor stem cell-derived migrasomes for enhanced bone regeneration. *Research.* 2026;9:1220. https://doi.org/10.34133/research.1220
9. Xiao H, Li W, Qin Y, Lin Z, Qian C, Wu M, *et al.* Crosstalk between lipid metabolism and bone homeostasis: exploring intricate signaling relationships. *Research.* 2024;7:0447. https://doi.org/10.34133/research.0447
10. Hassan MAM, Mohammed AH, Hameed EM. Application of Aloe vera gel blended polymer-collagen scaffolds for bone tissue engineering. *Nano Biomed Eng.* 2023;15:118–25. https://doi.org/10.26599/NBE.2023.9290016
11. Liu A, Yang G, Zhao Y, Deng J, Liu J, Zhang K, *et al.* Bone-targeted hybrid extracellular vesicles for alveolar bone regeneration. *Interdiscip Med.* 2025;3:e20240126. https://doi.org/10.1002/INMD.20240126
12. Xu C, Cheng P, Wang J, Zhang B, Shang P, Lv Y, *et al.* Unveiling the power of magnetic-driven regenerative medicine: bone regeneration and functional reconstruction. *Research.* 2025;8:0707. https://doi.org/10.34133/research.0707
13. Zhou J, Zhang Z, Joseph J, Zhang X, Ferdows BE, Patel DN, *et al.* Biomaterials and nanomedicine for bone regeneration: progress and future prospects. *Exploration (Beijing).* 2021;1:20210011. https://doi.org/10.1002/exp.20210011
14. Xiao P, Liu J, Du C, Cheng S, Liu S, Liu J, *et al.* Injectable mineralized hydrogel microspheres for accelerated osteocyte network reconstruction and intelligent bone regeneration. *J Control Release.* 2025;380:240–55. https://doi.org/10.1016/j.jconrel.2025.02.002
15. Haroun AA, Ayoob FA, Masoud RA. Sol-gel immobilization of colistin sulfate onto double walled carbon nanotubes: *in vitro* bone bioactivity. *Nano Biomed Eng.* 2024;16:498–509. https://doi.org/10.26599/NBE.2024.9290088
16. Zhao T, Chu Z, Ma J, Ouyang L. Immunomodulation effect of biomaterials on bone formation. *J Funct Biomater.* 2022;13:103. https://doi.org/10.3390/jfb13030103.
17. Yang L, Xu Z, Liu J, Chang X, Ren Z, Xiao WA. Multi-omics insights into bone tissue injury and healing: bridging orthopedic trauma and regenerative medicine. *Burns Trauma.* 2025;13. https://doi.org/10.1093/burnst/tkaf019.
18. Chen W, Zhang H, Zhou Q, Zhou F, Zhang Q, Su J. Smart hydrogels for bone reconstruction via modulating the microenvironment. *Research.* 2023;6:0089. https://doi.org/10.34133/research.0089
19. Zhang B, Su Y, Zhou J, Zheng Y, Zhu D. Toward a better regeneration through implant-mediated immunomodulation: harnessing the immune responses. *Adv Sci (Weinh).* 2021;8:e2100446. https://doi.org/10.1002/advs.202100446
20. Sui B, Ding T, Wan X, Chen Y, Zhang X, Cui Y, *et al.* Piezoelectric stimulation enhances bone regeneration in alveolar bone defects through metabolic reprogramming of

Downloaded from academic.oup.com/burnstrauma/article/doi/10.1093/burnst/tkag049/8742059 by guest on 12 October 2026

macrophages. *Exploration.* 2024;4:20230149. https://doi.org/10.1002/EXP.20230149
21. Su N, Villicana C, Yang F. Immunomodulatory strategies for bone regeneration: a review from the perspective of disease types. *Biomaterials.* 2022;286:121604. https://doi.org/10.1016/j.biomaterials.2022.121604
22. Sanati M, Pieterman I, Levy N, Akbari T, Tavakoli M, Hassani Najafabadi A, *et al.* Osteoimmunomodulation by bone implant materials: harnessing physicochemical properties and chemical composition. *Biomater Sci.* 2025;13:2836–70. https://doi.org/10.1039/d5bm00357a
23. Mooij I, Apachitei I, Zadpoor AA, Fratila-Apachitei LE. Biomaterial multiscale geometry for regenerative immunoengineering of bone tissue. *Acta Biomater.* 2025;203:21–37. https://doi.org/10.1016/j.actbio.2025.07.036
24. Rocha CV, Gonçalves V, da Silva MC, Bañobre-López M, Gallo J. PLGA-based composites for various biomedical applications. *Int J Mol Sci.* 2022;23:2034. https://doi.org/10.3390/ijms23042034.
25. Guo Y, Shi Z, Han L, Qin X, You J, Zhang Q, *et al.* Infection-sensitive SPION/PLGA scaffolds promote periodontal regeneration via antibacterial activity and macrophage-phenotype modulation. *ACS Appl Mater Interfaces.* 2024;16:41855–68. https://doi.org/10.1021/acsami.4c06430
26. Khabatova VV, Serov DA, Tikhonova IV, Astashev ME, Nagaev EI, Sarimov RM, *et al.* Selenium nanoparticles can influence the immune response due to interactions with antibodies and modulation of the physiological state of granulocytes. *Pharmaceutics.* 2022;14:2772. https://doi.org/10.3390/pharmaceutics14122772.
27. Yang Y, Liu Y, Yang Q, Liu T. The application of selenium nanoparticles in immunotherapy. *Nano Biomed Eng.* 2024;16:345–56. https://doi.org/10.26599/NBE.2024.9290100
28. Al-Shreefy HH, Al-Wasiti E, Al-Awady MJ. Investigation of encapsulated selenium nanoparticles with PLGA polymers against MCF-7 and HBL cell lines. *Nano Biomed Eng.* 2023;15:105–17. https://doi.org/10.26599/NBE.2023.9290013
29. Xu J, Tian Y, Zhu H, Peng B, Mo C. Ferroptosis and its emerging role in gestational diabetes mellitus. *Med Adv.* 2026;4:115–124. https://doi.org/10.1002/med4.70055
30. Liu J, Liu J, Liu S, Xiao P, Du C, Zhan J, *et al.* Cascade targeting selenium nanoparticles-loaded hydrogel microspheres for multifaceted antioxidant defense in osteoarthritis. *Biomaterials.* 2025;318:123195. https://doi.org/10.1016/j.biomaterials.2025.123195
31. Zou B, Xiong Z, Yu Y, Shi S, Li X, Chen T. Rapid selenoprotein activation by selenium nanoparticles to suppresses osteoclastogenesis and pathological bone loss. *Adv Mater.* 2024;36:e2401620. https://doi.org/10.1002/adma.202401620
32. Bai X, Zhou T, Wu X, Chang J, Wu X. Synthesis and application of selenium nanoparticles for the modulation of inflammatory diseases. *Nano Biomed Eng.* 2025;17:179–211. https://doi.org/10.26599/NBE.2025.9290111
33. Yadav D, Malviya R. Novel nanomaterials as photo-activated cancer diagnostics and therapy. *Med Adv.* 2023;1:190–209. https://doi.org/10.1002/med4.36
34. Liu H, Bian W, Liu S, Huang K. Selenium protects bone marrow stromal cells against hydrogen peroxide-induced inhibition of osteoblastic differentiation by suppressing oxidative stress and ERK signaling pathway. *Biol Trace Elem Res.* 2012;150:441–50. https://doi.org/10.1007/s12011-012-9488-4
35. Zhao G, Zhang Y, Tian Y, Huang J, Gao P, Zhao Q, *et al.* Antioxidant and anti-inflammatory effects of selenomethionine promote osteogenesis via Wnt/β-catenin pathway. *Biochem Biophys Rep.* 2023;36:101559. https://doi.org/10.1016/j.bbrep.2023.101559
36. Qin C, Wu C. Inorganic biomaterials-based bioinks for three-dimensional bioprinting of regenerative scaffolds. *VIEW.* 2022;3:20210018. https://doi.org/10.1002/VIW.20210018
37. Li C, Zhang W, Nie Y, Du X, Huang C, Li L, *et al.* Time-sequential and multi-functional 3D printed MgO(2)/PLGA scaffold developed as a novel biodegradable and bioactive bone substitute for challenging postsurgical osteosarcoma treatment. *Adv Mater.* 2024;36:e2308875. https://doi.org/10.1002/adma.202308875
38. Zou F, Jiang J, Lv F, Xia X, Ma X. Preparation of antibacterial and osteoconductive 3D-printed PLGA/Cu(I)@ZIF-8 nanocomposite scaffolds for infected bone repair. *J Nanobiotechnology.* 2020;18:39. https://doi.org/10.1186/s12951-020-00594-6
39. Zhang L, Yang G, Johnson BN, Jia X. Three-dimensional (3D) printed scaffold and material selection for bone repair. *Acta Biomater.* 2019;84:16–33. https://doi.org/10.1016/j.actbio.2018.11.039
40. Li X-R, Deng Q-S, Liu P-L, He S-H, Gao Y, Wei Z-Y, *et al.* Three-dimensional printed biomimetic multilayer scaffolds coordinated with sleep-related small extracellular vesicles: a strategy for extracellular matrix homeostasis and macrophage polarization to enhance osteochondral regeneration. *VIEW*. 2024;5:20230069. https://doi.org/10.1002/VIW.20230069
41. Qiao M, Wu W, Tang W, Zhao Y, Wang J, Pei X, *et al.* Applications and prospects of indirect 3D printing technology in bone tissue engineering. *Biomater Sci.* 2025;13:587–605. https://doi.org/10.1039/d4bm01374c
42. Skalny AV, Aschner M, Silina EV, Stupin VA, Zaitsev ON, Sotnikova TI, *et al.* The role of trace elements and minerals in osteoporosis: a review of epidemiological and laboratory findings. *Biomolecules.* 2023;13:1006. https://doi.org/10.3390/biom13061006.
43. Poleboina S, Sheth VG, Sharma N, Sihota P, Kumar N, Tikoo K. Selenium nanoparticles stimulate osteoblast differentiation via BMP-2/MAPKs/β-catenin pathway in diabetic osteoporosis. *Nanomedicine (Lond).* 2022;17:607–25. https://doi.org/10.2217/nnm-2021-0401
44. Tao ZS, Li TL, Wei S. Co-modified 3D printed β-tricalcium phosphate with magnesium and selenium promotes bone defect regeneration in ovariectomized rat. *J Mater Sci Mater Med.* 2023;34:7. https://doi.org/10.1007/s10856-022-06708-w
45. Gupte MJ, Swanson WB, Hu J, Jin X, Ma H, Zhang Z, *et al.* Pore size directs bone marrow stromal cell fate and tissue regeneration in nanofibrous macroporous scaffolds by mediating vascularization. *Acta Biomater.* 2018;82:1–11. https://doi.org/10.1016/j.actbio.2018.10.016
46. Chu L, Jiang G, Hu XL, James TD, He XP, Li Y, *et al.* Biodegradable macroporous scaffold with nano-crystal surface microstructure for highly effective osteogenesis and vascularization. *J Mater Chem B.* 2018;6:1658–67. https://doi.org/10.1039/c7tb03353b

Downloaded from academic.oup.com/burnstrauma/article/doi/10.1093/burnst/tkag049/8742059 by guest on 12 October 2026

47. Prasopthum A, Cooper M, Shakesheff KM, Yang J. Three-dimensional printed scaffolds with controlled micro-/nanoporous surface topography direct chondrogenic and osteogenic differentiation of mesenchymal stem cells. *ACS Appl Mater Interfaces.* 2019;11:18896–906. https://doi.org/10.1021/acsami.9b01472
48. Ding X, Zhang W, Xu P, Feng W, Tang X, Yang X, *et al.* The regulatory effect of braided silk fiber skeletons with differential porosities on *in vivo* vascular tissue regeneration and long-term patency. *Research (Wash D C).* 2022;2022:9825237. https://doi.org/10.34133/2022/9825237
49. Ye J, Xie C, Wang C, Huang J, Yin Z, Heng BC, *et al.* Promoting musculoskeletal system soft tissue regeneration by biomaterial-mediated modulation of macrophage polarization. *Bioact Mater.* 2021;6:4096–109. https://doi.org/10.1016/j.bioactmat.2021.04.017
50. Cui X, Xu L, Shan Y, Li J, Ji J, Wang E, *et al.* Piezocatalytically-induced controllable mineralization scaffold with bone-like microenvironment to achieve endogenous bone regeneration. *Sci Bull (Beijing).* 2024;69:1895–908. https://doi.org/10.1016/j.scib.2024.04.002
51. Yi L, Tang R, Shao C, Chen C, Tang J, Liao L, *et al.* A biodegradable zinc alloy membrane with regulation of macrophage polarization for early vascularized bone regeneration. *Biomater Res.* 2025;29:0223. https://doi.org/10.34133/bmr.0223
52. Chen H, Cheng R, Chung SH, Marghoub A, Zhong H, Fang G, *et al.* Direct ink writing of bioactive PCL/laponite bone implants: engineering the interplay of design, process, structure, and function. *BMT.* 2025;11:100101. https://doi.org/10.1016/j.bmt.2025.100101
53. Feng J, Liu J, Wang Y, Diao J, Kuang Y, Zhao N. Beta-TCP scaffolds with rationally designed macro-micro hierarchical structure improved angio/osteo-genesis capability for bone regeneration. *J Mater Sci Mater Med.* 2023;34:36. https://doi.org/10.1007/s10856-023-06733-3
54. Zhou H, Li Z, Jing S, Wang B, Ye Z, Xiong W, *et al.* Repair spinal cord injury with a versatile anti-oxidant and neural regenerative nanoplatform. *J Nanobiotechnology.* 2024;22:351. https://doi.org/10.1186/s12951-024-02610-5
55. Qin D, Zhao Y, Cheng R, Liu Y, Guo S, Sun L, *et al.* Mussel-inspired immunomodulatory and osteoinductive dual-functional hydroxyapatite nanoplatform for promoting bone regeneration. *J Nanobiotechnology.* 2024;22:320. https://doi.org/10.1186/s12951-024-02593-3
56. Li X, Wen ZY, Song JX, Tang H, Liu WS, Linghu X, *et al.* Three-dimensional-printed hydroxyapatite/nanoclay/polycaprolactone composite scaffold for immunomodulation and bone defect repair. *Int J Bioprint.* 2025;11:434–56. https://doi.org/10.36922/ijb025170162.
57. Huang D, Li Z, Li G, Zhou F, Wang G, Ren X, *et al.* Biomimetic structural design in 3D-printed scaffolds for bone tissue engineering. *Mater Today Bio.* 2025;32:101664. https://doi.org/10.1016/j.mtbio.2025.101664
58. Cheng S, Yang L, Dong M, Luo X, Zhang X, Zhai Y, *et al.* Metabolism-regulating microspheres: design principles, therapeutic applications across multisystem diseases, and future perspectives. *Research (Wash D C).* 2026;9:1106. https://doi.org/10.34133/research.1106
59. Wan Y, Zhang W, Liao Y, Zhu C, Guo X, Zou Z, *et al.* Nanotechnology and cell death: revolutionizing disease treatment with nanoparticle strategies. *VIEW.* 2025;6:20250033. https://doi.org/10.1002/VIW.20250033
60. Wen-qing HU, SHI J-f, Yuan LU, Huan-gan WU, Guo-na LI, YIN X-l, *et al.* Moxibustion modulates gut microbiota and improves bone marrow hematopoiesis in mice with myelosuppression-induced aplastic anemia. *World J Acupunct Moxibustion.* 2025;35:357–66. https://doi.org/10.1016/j.wjam.2025.09.003
61. Fatima S, Alfrayh R, Alrashed M, Alsobaie S, Ahmad R, Mahmood A. Selenium nanoparticles by moderating oxidative stress promote differentiation of mesenchymal stem cells to osteoblasts. *Int J Nanomedicine.* 2021;16:331–43. https://doi.org/10.2147/ijn.S285233
62. Gao G, Li J, Ma Y, Xie M, Luo J, Wang K, *et al.* Dual-responsive multi-functional silica nanoparticles with repaired mitochondrial functions for efficient alleviation of spinal cord injury. *Exploration.* 2025;5:270012. https://doi.org/10.1002/EXP.70012
63. CHEN S-l, HUANG L-h, BIAN Y-h, WANG Y-m, ZHANG J-y, LIAN J-y, *et al.* Acupuncture therapy: a potential new strategy for immunosuppressive sepsis. *World J Acupunct Moxibustion.* 2025;35:17–26. https://doi.org/10.1016/j.wjam.2024.03.001
64. Xu RH, You YY, Zheng WY, Ma L, Chang YZ, Pan SY, *et al.* Selenoprotein-regulated hydrogel for ultrasound-controlled microenvironment Remodeling to promote bone defect repair. *Adv Funct Mater.* 2024;34:2313122. https://doi.org/10.1002/adfm.202313122.
65. Chen Y, Xu R, Xie B, Ma L, He Y, Liu H, *et al.* Ultrasound-driven selenium nanoparticles realize bone defect repair through activating selenoproteins to regulate PI3K/AKT signaling pathway. *ACS Nano.* 2025;19:18256–69. https://doi.org/10.1021/acsnano.4c18240
66. Xiao J, Cao H, Guo S, Xiao S, Li N, Li M, *et al.* Long-term administration of low-dose selenium nanoparticles with different sizes aggravated atherosclerotic lesions and exhibited toxicity in apolipoprotein E-deficient mice. *Chem Biol Interact.* 2021;347:109601. https://doi.org/10.1016/j.cbi.2021.109601
67. Singh H, Kaur J, Datusalia AK, Naqvi S. Age-dependent assessment of selenium nanoparticles: biodistribution and toxicity study in young and adult rats. *Nanomedicine (Lond).* 2023;18:2021–38. https://doi.org/10.2217/nnm-2023-0204
68. Ferroudj A, Muthu A, Sári D, Törős G, Beni Á, Czeglédi L, *et al.* Comparative study of red and grey selenium nanoparticles on organ-specific selenium deposition and growth performance in Japanese quails. *Nanomaterials (Basel).* 2025;15:801. https://doi.org/10.3390/nano15110801

Downloaded from academic.oup.com/burnstrauma/article/doi/10.1093/burnst/tkag049/8742059 by guest on 12 October 2026

© The Author(s) 2026. Published by Oxford University Press. This is an Open Access article distributed under the terms of the Creative Commons Attribution-NonCommercial License (https://creativecommons.org/licenses/by-nc/4.0/), which permits non-commercial re-use, distribution, and reproduction in any medium, provided the original work is properly cited. For commercial re-use, please contact reprints@oup.com for reprints and translation rights for reprints. All other permissions can be obtained through our RightsLink service via the Permissions link on the article page on our site—for further information please contact journals.permissions@oup.com.
Burns & Trauma, 2026, 14, tkag049
https://doi.org/10.1093/burnst/tkag049
Research Article